Thesis for the degree of Licentiate of Engineering

High temperature properties of polycrystalline $Mo(Si,Al)_2$: compression and oxidation

Aina Edgren

Department of Physics

Chalmers University of Technology

Gothenburg, Sweden 2021

High temperature properties of polycrystalline $Mo(Si,Al)_2$:
compression and oxidation

Aina Edgren

Department of Physics
Chalmers University of Technology
SE-412 96 Gothenburg
Sweden
Telephone + 46 (0)72-231 9801

Cover illustration
Left: KAM and GROD maps and misorientation profiles of deformed $Mo(Si,Al)_2$.
Right: BSE image of Al_2O_3 grain in oxide scale with YS dendrites.

Printed by Chalmers Reproservice
Gothenburg, Sweden 2021

High temperature properties of polycrystalline $Mo(Si,Al)_2$:
compression and oxidation
Aina Edgren
Department of Physics
Chalmers University of Technology

Abstract

Electrification of industrial heating processes holds great promise for reducing CO_2 emissions. Large furnaces operating at elevated temperatures and in demanding atmospheres are complicated but indeed important to electrify. A material often used as heating elements in small-scale furnaces operating in harsh environments is $Mo(Si,Al)_2$, hence, the material is a high-potential candidate for the electrification of more complicated industrial heating processes. Such applications require $Mo(Si,Al)_2$ heating elements with increased dimensions, which poses new challenges with respect to the high temperature performance of the material.

With increasing element size, the mechanical properties are expected to become more important. In this thesis, the mechanical response and the resulting microstructure of polycrystalline $Mo(Si,Al)_2$, tested in compression at 1300 °C, was investigated. The main findings were: (1) the material could sustain large plastic strains without cracking, (2) the deformation was inhomogeneous on both intra- and intergranular scale, and low angle grain boundaries were formed in severely deformed grains, (3) the material softens due to dynamic recrystallisation.

In spite of the excellent oxidation and corrosion resistance of $Mo(Si,Al)_2$, there are indications that oxide spallation could present a potential issue for larger heating element dimensions. In this thesis, the effect of reactive element addition, which is known to effectively reduce spallation in e.g. FeCrAl alloys, was investigated. $Mo(Si,Al)_2$ was alloyed with yttrium and exposed at 1500 °C for up to 250 h. The study showed that (1) oxide adhesion was not improved, as the oxide scale spallation increased with increasing yttrium content, (2) also the oxidation rate increased with yttrium addition, (3) yttrium silicate and mullite were formed from a melt within the otherwise pure alumina scale.

Keywords: $Mo(Si,Al)_2$, hot compression, mechanical properties, microstructure, oxidation, heating element, reactive element, Gleeble

Preface

The research work presented in this licentiate thesis was carried out at the Division of Microstructure Physics at the Department of Physics, Chalmers University of Technology and at the Research and Development division of Kanthal AB, during the time period October 2019 - December 2021, under the supervision of Associate Professor Magnus Hörnqvist Colliander (Chalmers University of Technology) and Doctor Erik Ström (Kanthal AB).

This research is funded by the Swedish Foundation for Strategic Research (SSF) and Kanthal AB, through the industrial PhD student grant ID18-0064.

List of appended papers

I. *Influence of Yttrium Doping on the Oxidation of Mo(Si,Al)$_2$ in Air at 1500 °C*
Aina Edgren, Lars-Gunnar Johansson, Erik Ström, Magnus Hörnqvist Colliander
In Manuscript.

II. *High temperature deformation of polycrystalline C40 Mo(Si,Al)$_2$*
Aina Edgren, Erik Ström, Lars Frisk, Farid Akhtar, Magnus Hörnqvist Colliander
In Manuscript.

My contributions to the appended papers

I. I performed the oxidation exposures of the samples which were later investigated in scanning electron microscope. I did the microstructure analysis, analysed and evaluated the data and wrote the paper.

II. I synthesised the $Mo(Si,Al)_2$ material and prepared the testing specimens. I developed and conducted the high-temperature compression testings with assistance from Lars Frisk (Luleå University of Technology) and Farid Akhtar (Luleå University of Technology), I did the microstructure analysis, analysed and evaluated the data and wrote the paper.

Acknowledgements

First and foremost I would like to thank my supervisors, Prof. Magnus Hörnqvist Colliander and Dr. Erik Ström, not only for giving me the opportunity to pursue this interesting PhD project but mainly for their tremendous support. A special thanks to Magnus for his outstanding guidance and to Erik for his expertise within the high-temperature ceramics field and for inspiring discussions.

I am also grateful for all my colleagues at Chalmers and Kanthal, I have enjoyed all the interesting conversations in the coffee rooms. A special thanks to Emil Eriksson and Dr. Anand H.S. Iyer for introducing me to EBSD, and to Dr. Stefan Gustafsson and Dr. Ludvig de Knoop at CMAL for instant support with the microscopes. Many thanks to Jörgen Sahlström and Toni Syrjälä for helping me with materials synthesis in the lab. I am also grateful to Prof. Farid Akthar and Lars Frisk at Luleå University of Technology for helping me with the compression testings.

I will also take this opportunity to thank my former colleges at the division of Environmental Inorganic Chemistry Tommy Sand, Dr. Christine Geers and Prof. Lars-Gunnar Johansson for introducing me to high-temperature corrosion and the research world in general, during my master's thesis work in 2019. Without you I had not been a PhD student today.

Last but not least, I would like to thank my family and friends for always supporting me. Special thanks to Henrik for his love and for always being there for me when things get tough.

Contents

CHAPTER 1

Introduction

1.1 The need for electrification of industrial heating processes

Global warming is one of the most difficult challenges facing the world today. If the emission of greenhouse gases are not decreased drastically within the near future, the global mean temperature will continue to increase, with melting of the polar ice caps and extreme weathers as results. In 2016, almost 200 parties signed the Paris agreement, with the long term goal of keeping the increase in global mean temperature below 2 °C, compared with pre-industrial levels [1].

The main cause of global warming is the emission of greenhouse gasses. As can be seen in Figure 1.1, the energy sector counts for almost three-quarters of the total emission [2], the industry is the largest sub-sector and 7.2 % of the total greenhouse gas emission comes from the iron and steel industry [2]. Due to the high temperatures needed, this industry is a very challenging sector to electrify, but attempts are being made already today. One example is the Swedish project HYBRIT [3], which aims to develop a completely fossil-fuel free steel-making process. One of the first steps in the steel-making is to reduce the iron-ore to iron. Traditionally, this has been done using coking coal and is associated with very high CO_2 emissions. In the HYBRIT project,

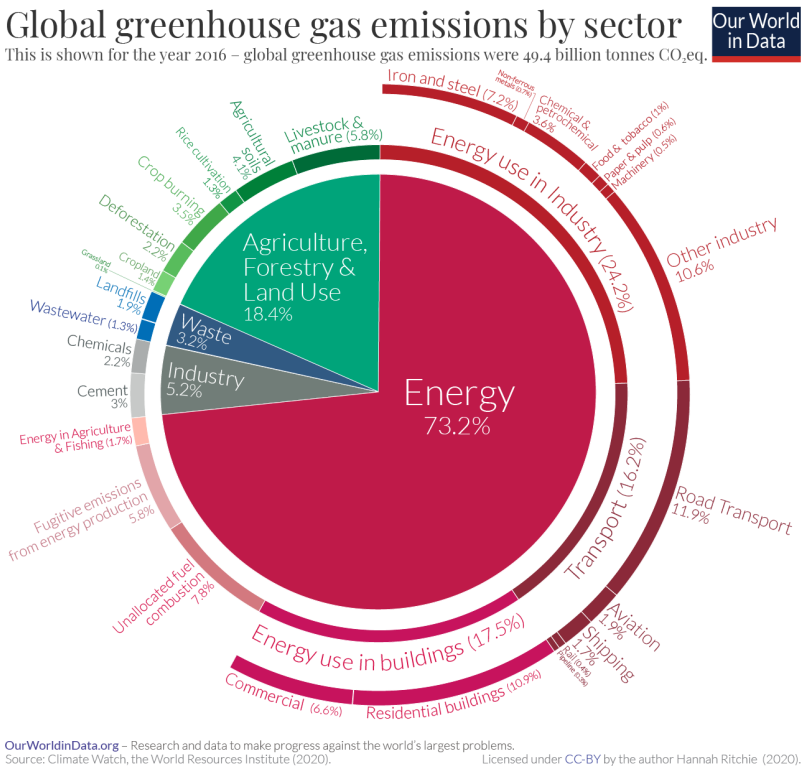

Figure 1.1: Global greenhouse emissions by sector. Licenced under CC-BY by Hannah Ritchie [2]

the much more environmentally friendly hydrogen gas, which can be produced from electricity and water, is used instead [3].

In a paper by Madeddu *et al.* [4], the energy use within the industrial sector was studied more in detail. It was shown that the chemicals, primary steel and paper industries together use 70 % of the total energy. 45 % of the energy is used as heat, of which 18 % is used for high-temperature heating (above 1000 °C). Within the primary steel sector, the high-temperature heating counts for the majority of the energy used, see Figure 1.2 [4]. Furthermore, 36 % of the energy comes from fossil fuels [4], hence, electrification of such processes is therefore critically important in order to reduce the CO_2 emission.

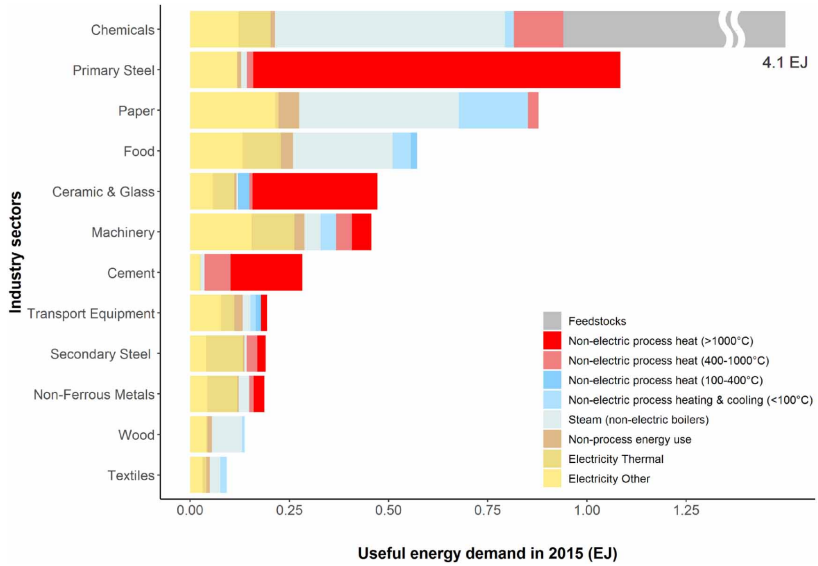

Figure 1.2: Distribution of industry useful energy demand for the year 2015 in 27 EU member states and United Kingdom. "Figure 1" by Madeddu *et al.* [4] licensed under CC BY 4.0

1.2 Resistive heating as a solution

Different types of electric heating systems exists, e.g. resistance (or joule) heating and induction heating. The research done in this thesis is focused on the resistance heating, more specifically, the material used for such systems. Resistance heating is a mature technology having many advantages. With its rapid heating rate and high controllability it is be used in a wide range of applications, including heat treating metals and household appliances [5], two examples are shown in Figure 1.3. Furthermore, the technology has a high efficiency and low maintenance [5]. It is therefore believed that this technology will play a key role in the electrification of e.g. the steel industry.

The systems based on resistance heating typically consist of one or several heating elements, through which a current is flowing. The elements, which are directly heated, indirectly heat (by radiation, convection or conduction) the furnace and the products placed in it [5]. Using Ohm's law,

$$V = IR \tag{1.1}$$

and the relation

$$P = IV = I^2R$$

where V is the applied potential, I the current, R the resistance and P the

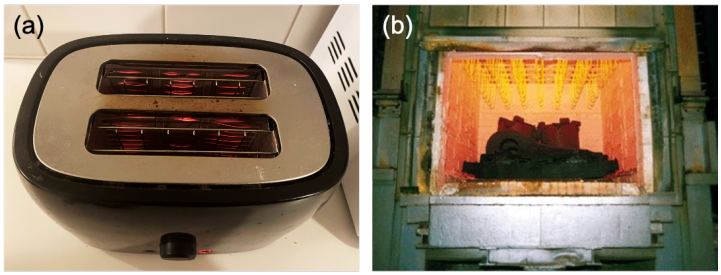

Figure 1.3: Heating elements used in (a) toaster, (b) industrial furnace

power, the heat, Q, obtained from a heating element (having diameter A and length l) can be calculate,

$$Q = I^2Rt = \rho\frac{l}{A}I^2t \tag{1.2}$$

As seen from Equation 1.2, the heat generated is proportional to ρ, the resistivity of the material, hence, a material used for heating element should have high resistivity. However, if the resistance is too high, the material is an insulator and can not be used. Typical heating element materials are ferritic alloys (e.g. FeCrAl), austenitic alloys (e.g. NiCr) and ceramics (e.g. $MoSi_2$ and $Mo(Si,Al)_2$), the resistivity and typical maximum operation temperatures are shown in Figure 1.4. Observed from the figure is that the two ceramic materials have higher resistivity (at high temperatures) than the alloys and that $Mo(Si,Al)_2$ has a more planar resistivity-temperature relationship than $MoSi_2$. This makes it easier to control the temperature of the $Mo(Si,Al)_2$ element.

In addition to the resistivity and operating temperature, atmosphere and size requirements are other important factors to consider when selecting a material for the heating element. The metal based heating elements are used with success in both household equipment and industrial furnaces, they are relatively cheap and easy to produce. However, in challenging environments, e.g. at very high temperature and in reducing atmosphere, molybdenum aluminosilicide, $Mo(Si,Al)_2$, is often a better alternative. The material has a high melting point and excellent oxidation behaviour in different atmospheres.

As mentioned, electrification of high-temperature industrial processes, e.g. within the steel industry, is important in order to reduce the CO_2 emissions. It is believed that $Mo(Si,Al)_2$ is a promising material for such heating elements. However, the $Mo(Si,Al)_2$ elements used today are developed to operate in the kW scale, while the new applications require much higher heating powers. To meet the requirements, the dimensions, e.g. the diameter, of the heating elements need to be larger. The up-scaling results in elements having higher mass, furthermore it is expected that the elements need to be mounted in

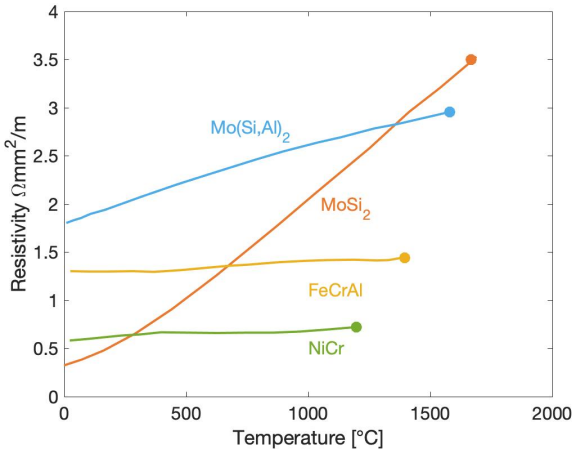

Figure 1.4: Resistivity as a function of temperature of four different heating element types. The filled circles indicates the maximum operating temperature. The figure is based on data from [6] and [7]

a horizontal position to uniformly heat large volumes, which may challenge the mechanical properties. The larger diameter may also affect the oxidation properties, e.g. oxide scale adhesion.

1.3 Aim of this thesis

This PhD project is one part of a collaboration between the heating element producer Kanthal AB and Chalmers University of Technology (Department of Physics). The long-term goal of the collaboration is to facilitate the development of the next generation high temperature ceramic heating elements for application in extreme environments. The overall aim of the PhD project is to deepen the knowledge regarding the mechanical properties of $Mo(Si,Al)_2$. The effect of particle strengthening and alloying with other element, such as Nb, Ta, and V will be investigated.

Very limited research has been done on mechanical properties of $Mo(Si,Al)_2$ based materials prior to this project, and the research has mainly focused on single crystals. Because of the much more complicated stress state (due to i.e. orientation of grains, effect of grain boundaries etc.) in polycrystalline samples compared with single crystals, it is important to first understand the deformation mechanisms taking place in an unalloyed, polycrystalline $Mo(Si,Al)_2$ material. In this licentiate thesis, $Mo(Si,Al)_2$ has been synthesised and a method for testing the high temperature mechanical properties has been developed.

The microstructure of the material has been investigated using scanning electron microscopy (SEM) based methods, such as electron backscatter diffraction (EBSD) and Energy dispersive X-ray spectroscopy (EDS). The results from this study will form the basis for future research involving particle strengthening and alloying elements. The research question to be answered in this work is

- How does the microstructure of polycrystalline $Mo(Si,Al)_2$ evolve when tested in compression at high temperature?

Based on internal communications at Kanthal, also the oxide adhesion on $Mo(Si,Al)_2$ may be affected by an increase in element diameter. If this is true, the oxidation properties may need to be tuned for the new applications. One way to improve the oxide scale adhesion in metallic materials (e.g. FeCrAl) is to alloy with small amounts of reactive elements, e.g. Y and Zr. In this thesis, following reserach question is to be ansvered

- Can Y-alloying be used to improve the oxidation properties of $Mo(Si,Al)_2$?

CHAPTER 2

Structure and properties of molybdenum (alumino)silicides

$MoSi_2$ and $Mo(Si,Al)_2$ can be used as heating elements operating at high temperatures. However, the current versions of the elements are not designed to generate heating power in the MW scale, which might be needed for the applications in large, high-temperature industrial furnaces in the future. It is possible that both the mechanical and oxidation properties need to be improved in order to meet the requirements, hence, the properties of the materials used today must be thoroughly understood. In this chapter, the results of a literature study, summarising the properties of $MoSi_2$ and $Mo(Si,Al)_2$ based materials, is presented.

2.1 General characteristics of ceramic materials

There is no strict definition of the material group called ceramic materials [8], but a common description is "a material that is neither a metal nor a plastic" [9]. Due to this broad and vague description, ceramic materials are often divided into different classes such as engineering ceramics, glass, pottery and cement. The classes can further be divided into several sub-classes, e.g. the engineering ceramics contains sub-classes such as metal oxide compounds (e.g.

SiO_2 and Al_2O_3) and non oxide compounds (e.g. SiC, $MoSi_2$ and $Mo(Si,Al)_2$) [8].

With properties such as high hardness, high stiffness and often high-temperature tolerance, ceramic materials can be used for a variety of applications. However, the most characteristic property of ceramics may be the high brittleness, which often limits the use of the material [8]. A typical, polycrystalline, ceramic sample does not show any plastic deformation at all before fracture if stressed at ambient temperature. Figure 2.1 shows typical stress-strain curves for three different types of materials: ceramics, metals and polymers. As can be seen, the metal undergoes both elastic and plastic deformation, while the ceramic fractures after a very small elastic strain.

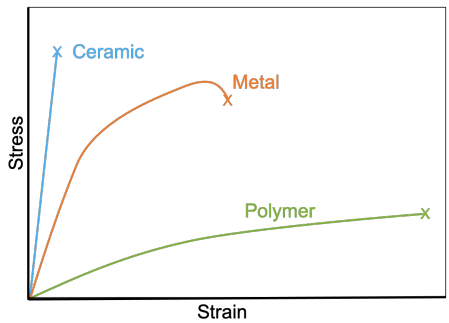

Figure 2.1: Typical stress-strain curves for a ceramic, metal and polymer

The main difference between ceramics and metals when it comes to deformation is that the dislocation activity is restricted in ceramics, while in metals they can move more easily [8, 9]. When a dislocation is moving in a ceramic, bonds need to be broken and new ones created. In ceramic materials, the bonds between the atoms can be covalent or ionic (often a mix of the two types) and are often both strong and directional. In metals, where the electrons are delocalised and the bonds are non-directional, the dislocations can move with relative ease [8, 9].

Another difference between the two types of materials is the complexity of the unit cell [8, 9]. While metals and alloys often have rather simple unit cells such as fcc (face centred cubic), ceramics often have large unit cells with low symmetry consisting of at least two types of atoms. As a consequence, the Burgers vector (which describes the direction and magnitude of the slip caused by a dislocation) tends to be large in ceramics. Since the strain energy is proportional to the square of the magnitude of Burgers vector, the energy needed for dislocation nucleation in ceramics is much higher than in metals [8, 9]. Due to the difficulty in activating multiple slip systems, ceramic materials

do not usually fulfill the von Mises criterion (five independent slip systems are required to deform a material uniformly), hence, polycrystalline ceramic materials often fail in a brittle manner rather than yield.

2.2 Silicides

One technologically important group of ceramics is the metal-silicides. As the name reveals, the group contains intermetallic compounds of silicon and a metal, such as Mo, Nb, W, Cr or Ti. Silicides are not new materials but have been subjects of research for over 100 years [10], first as high-temperature corrosion-protective coatings, but later also as bulk materials for structures at temperatures too high for Ni-based superalloys. The materials are well suited for elevated temperatures due to high melting point (often above 2000 °C) and excellent corrosion resistance. However, just like other ceramic materials, silicides do have some drawbacks when it comes to mechanical behaviours. The ductile to brittle transition temperature (DBTT) is high, making the materials very brittle at low temperatures. Above the DBTT, the material suffers from softening. These behaviours limit the use of the material. A lot of research is done to improve the high-temperature strength of the materials.

In the following chapters, the crystal structures, the deformation mechanisms at both high and low temperatures, as well as the oxidation behaviour of the silicides will be discussed. The main focus will be on $MoSi_2$ and $Mo(Si,Al)_2$, but some of the other silicides will also be mentioned for a broader understanding. Even though the metal used in the different silicides may differ, many of the properties are similar.

2.2.1 Mo based silicides

Molybdenum silicides are some of the most studied silicides. Three different intermetallic compounds can be found within the Mo-Si phase diagram (Figure 2.2), the highly stoichiometric line-compounds $MoSi_2$ and Mo_3Si, and Mo_5Si_3, having a narrow solubility range of 3 at.% Si. $MoSi_2$ has a body-centered tetragonal crystal structure, called $C11_b$, which is built up by ABAB stacking of (001) planes, see Figure 2.3(a) [11]. The c/a ratio is 2.452. The strong and directional -Si-Mo-Si- chains, as well as -Mo-Si-Si-Mo- chains, are along the [001] direction, which will be very important when the deformation mechanisms of the material will be discussed later on. The $C11_b$ structure is stable up to 1900 °C. Above this temperature the hexagonal C40 structure (Figure 2.3(b)) is stable up to 2030 °C, which is the melting point of the material [10–12] The stacking sequence of the (0001) planes in the C40 phase is ABCABC.

This stacking sequence is the same as that of the (110) planes within $C11_b$.

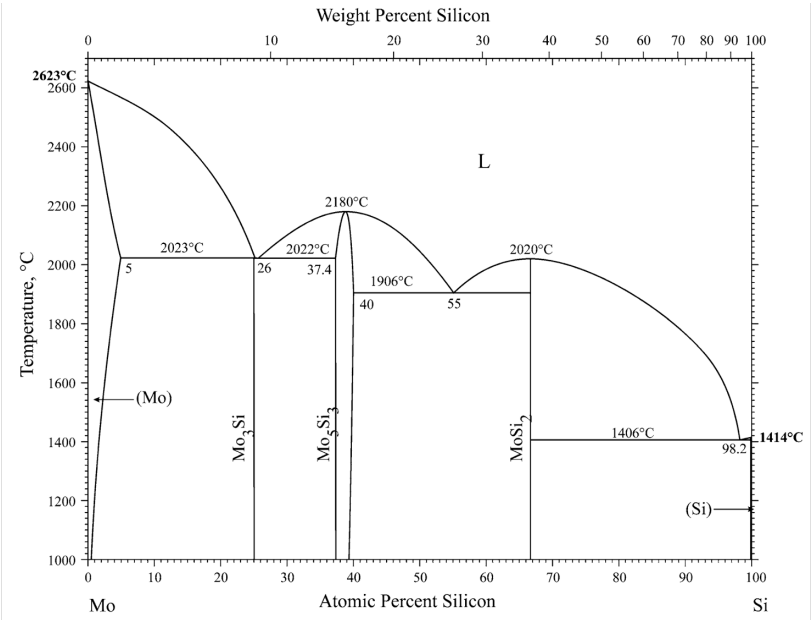

Figure 2.2: Mo-Si phase diagram. Acquired from [13] with permission

Mo_5Si_3 has a tetragonal structure called $D8_m$ (Figure 2.3(c)), but in contrast to $C11_b$, the a-lattice parameter is larger than the c-lattice parameter (a/c=2). In this structure, the -Si-Mo-Si- chains are along the [010] and [100] directions. The CTE (coefficient of thermal expansion) of Mo_5Si_3 is very anisotropic. That means that the crystal will not expand homogeneously if heated [14].

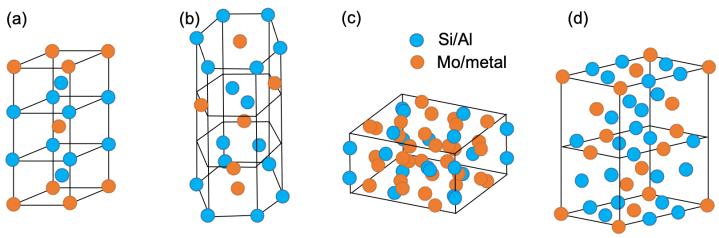

Figure 2.3: Crystal structures of (a) $C11_b$, (b) C40 (c) $D8_m$, (d) C54

$MoSi_2$ can be alloyed with several elements, such as Nb, W, Al, and Cr, in order to tune the properties of the material. The most important alloying element in this work is Al. If the Al addition is less than 3 at.% the $C11_b$ structure is retained, but a higher alloying fraction leads to stabilisation of C40 structured $Mo(Si,Al)_2$ [15, 16]. The C40 material is stoichiometric, meaning

that Al atoms substitute Si to keep the Mo:(Si,Al) ratio 1:2. The more precise composition is often written as $Mo(Si_{2-x}Al_x)$ where $0.2< x <2$. If the Al content is higher (around 33 at.%), an additional phase becomes stable in the multi-phase material, the orthorhombic C54 [17]. C54 is often denoted as $Al_{13}Mo_{10}Si_7$, but is stable even with a Al concentration of 38 at.%, which is 5 at.% lower than the stoichiometric content [17]. The C54 crystal structure is shown in Figure 2.3(d).

In addition to $Mo(Si,Al)_2$, and $MoSi_2$ at very high temperature, also some other silicides, $NbSi_2$, VSi_2, $TaSi_2$ and $CrSi_2$, have the C40 structure. Even though they do not contain Mo, it is worth mentioning these materials because the mechanical behaviour, which will be discussed in the next chapter, is similar to that of $Mo(Si,Al)_2$.

2.2.2 $Mo(Si,Al)_2$ based multiphase material

When producing ceramic materials in lab scale the processes can be highly controlled, resulting in a material having low contamination levels and no unwanted phases. If instead the material is produced in a larger scale, it is not possible to maintain the same control. As mentioned in the introduction to this thesis, $Mo(Si,Al)_2$ is often used as electrical heating elements. One example is the material Kanthal® Super ER, which is produced in a relatively large scale. In addition to the main C40 structured $Mo(Si,Al)_2$ phase (81 vol.%), the material also contains Al_2O_3 (13 vol.%) and $D8_m$ structured $Mo_5(Si,Al)_3$ (6 vol.%) [18]. The chemical composition of the $Mo(Si,Al)_2$ phase is approximately 34 at.% Mo, 35 at.% Si and 27 at.% Al. The oxidation behavior of this material has been extensively studied, e.g. by Ingermarsson *et al.* [18–21], but not much has been published regarding the mechanical properties.

2.3 Mechanical behaviour of silicides at low temperature

At low temperatures, all silicides have a brittle behaviour. The fracture toughness values of $MoSi_2$ lies in the range of 1.9-5.3 $MPa\sqrt{m}$ for both single and polycrystalline materials [11], typical values for metals and alloys are 10-200 $MPa\sqrt{m}$ [22]. The main reason for the very low fracture toughness is the directionality of the bonds. By alloying $Mo(Si,Al)_2$ with Al, the fracture toughness is expected to be improved due to the formation of metallic Mo-Al bonds [11]. Mitra *et al.* [23] tested the fracture toughness of polycrystalline $MoSi_2$ alloyed with different Al content. For materials where only the $C11_b$ structure and small amounts of SiO_2 were present, the fracture toughness was just modestly improved from 4.3 $MPa\sqrt{m}$ (unalloyed $MoSi_2$) to 4.67 $MPa\sqrt{m}$. For a material

with higher Al contents, in which both $C11_b$, C40 and Al_2O_3 were present, the fracture toughness at room temperature was 6.4 MPa$\sqrt{m}$ [23]. Even though Al alloying lead to improved properties, the changes were small [11, 23].

Another way to improve the fracture toughness of polycrystalline silicides is to add reinforcements. For $MoSi_2$, SiC particles and whiskers, as well as partially stabilised ZrO_2 particles, have been used to improve the low-temperature mechanical properties. Such reinforcements often lead to an improvement of fracture toughness to about 5-10 MPa$\sqrt{m}$ [11].

2.4 Mechanical properties of silicides at high temperature

If a material is deformed at a temperature higher than the DBTT, plastic deformation is possible. The DBTT of polycrystalline $MoSi_2$ and $Mo(Si,Al)_2$ lies above 1000 °C, but is highly dependent on the type of grain size, strain rate and impurity level. In the following sections, the mechanical properties of $MoSi_2$ and $Mo(Si,Al)_2$ at high temperature are presented. Properties of other silicides are briefly discussed.

2.4.1 $MoSi_2$

In $MoSi_2$ with $C11_b$ structure, plastic deformation of single crystals is possible at low temperature but is highly dependent on the orientation of the crystal. In total, five independent slip systems have been identified in $MoSi_2$: $\{110\}\langle 111]$[1], $\{011\}\langle 100]$, $\{010\}\langle 100\rangle$, $\{023\}\langle 100]$ and $\{013\}\langle 331]$ [24].

Ito *et al.* [24] have reported that plastic deformation of single crystals, oriented away from the [001] direction, is possible at temperatures as low as room temperature. The active slip systems at room temperature are $\{011\}\langle 100]$ or $\{013\}\langle 331]$, depending on the sample orientation. Above 300 °C, the $\{110\}\langle 111]$ system can be active, and above 800 °C, $\{023\}\langle 100]$ has been identified. The $\{010\}\langle 100\rangle$ system in single crystals was found to be active only in some orientations and only within a temperature range of 600-900 °C. If the sample is oriented with the [001] direction along the stress axis, Ito *et al.* found that plastic deformation was only possible above 1300 °C [24]. Other research groups, e.g. Maloy *et al.* [27], have reported that a single crystal oriented in this direction deforms at lower temperatures (above 1000 °C). It is possi-

[1]The mixed notation are often used for the C11b structured $MoSi_2$ to differentiate the first two indices from the third index which does not play the same role as the first two because of the tetragonality [24–26]

ble that the difference in temperature reported can be explained by the very orientation-dependent behaviour of the $\{013\}\langle 331]$ slip system. If the crystal is tilted just a few degrees away from the exact [001] orientation, the critical resolved shear stress (CRSS) of this slip system decreases significantly [11, 24, 28], hence, deformation at temperatures lower than 1300 °C could be possible. Normally, CRSS of a slip system do not change with orientation. However, in the present case, it might be be possible due to dissociation and decomposition of the dislocations operating in this slip system [11, 24, 27–29].

When it comes to the creep behaviour of single crystals, the trends are similar to those discussed in case of deformations at constant strain rates. For example, [001] oriented crystals have much higher creep resistance than other orientations [11].

The DBTT for polycrystalline $MoSi_2$ has been reported to lie between 1000 and 1300 °C [11, 24, 28, 30]. As has been discussed earlier, the $\{013\}\langle 331]$ slip system for crystals having the exact [001] orientation becomes active first at a temperature of 1300 °C. At or below 1000 °C, only four independent slip systems are active, which is less than the five independent slip systems considered necessary for homogeneous deformation of polycrystalline samples (Von Mieses criterion). Therefore, only grains oriented away from the [001] orientation can be deformed. It is possible that dislocation climb and grain boundary diffusion could be used to explain why some research groups have reported ductile behaviour of polycrystalline $MoSi_2$ below 1300 °C [11, 24]. Furthermore, the stress state in polycrystalline materials is very complicated. Grains oriented in a non-favourable direction relative to the external stress direction may deform due to stresses arising from neighbouring grains. The lower DBTT reported may also be a result of high oxygen impurities, leading to the formation of SiO_2 particles at grain boundaries [31]. At elevated temperatures, the softening of these particles promotes grain boundary sliding and localised deformation [31].

In addition to impurity level, also the grain size, alloying, reinforcement, strain rate and temperature are important when discussing the high-temperature mechanical properties. Mitra *et al.* [31] have studied compression of two different $MoSi_2$ materials at temperatures between 1000 and 1350 °C using different strain rates. The SiO_2 content, as well as the grain size, differed between the two materials. For both materials, the yield stress and the maximum stress decreased with increasing temperature due to thermal activation of dislocation movements [31], see the stress-displacement curve from of two materials in Figure 2.4. The effect was most pronounced in case of the fine-grained material. At lower temperatures (and at high temperatures if the strain rate was low), the fine-grained material had the highest strength. This is in line with

the Hall-Petch equation [31],

$$\sigma_y = \sigma_0 + k/\sqrt{d} \tag{2.1}$$

where σ_y is the yield stress, σ_0 and k are material constants and d is the grain diameter, which indicates that a reduction in grain size leads to an increase in yield stress. The effect is due to the large area of grain boundaries, acting as obstacles for dislocation movements. $MoSi_2$ follows the Hall-Petch relationship from room temperature up to 1000 or 1200 °C (the exact temperature depends on strain rate, grain size, impurity level etc. [31]). At higher temperatures, the flow stress has been shown to decrease with increased temperature, see Figure 2.4. This phenomenon, where the yield stress increases with temperature up to a certain point, and after that decreases, is called anomalous strengthening and has been observed in $C11_b$ by several research groups [11, 15, 28, 29].

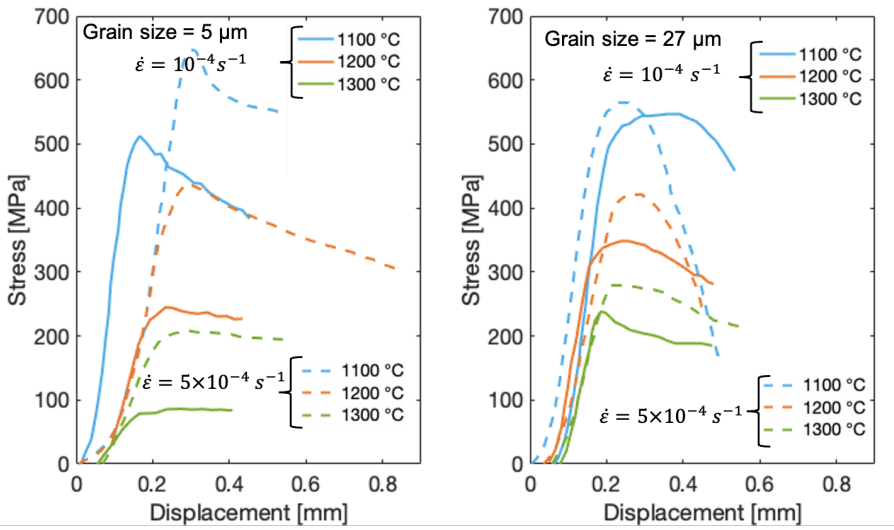

Figure 2.4: The effect of temperature and strain rate of $MoSi_2$ having different grain size: (a) 5 μm, (b) 27 μm The figures are based on data from [31]

Mitra *et al.* also showed the $MoSi_2$ grain size affects the rate of strain hardening of the material [31], see Figure 2.4. In a fine-grained material, the dislocation density is often higher due to the large grain boundary area. If the strain rate is high, or the temperature is low, the ability for diffusion at grain boundaries (which leads to recovery and softening) is low, leading to a high strain hardening rate [31]. If the temperature is increased, or the strain rate is reduced, diffusion is enhanced and dislocation can annihilate more easily. The strain hardening rate decreases as a result. In addition, the dislocations can rearrange themselves into low angle grain boundaries (LAGB) within the grains, leading to a decrease in strain hardening rate [31].

The presence of SiO_2 particles, which soften and promote grain boundary sliding of $MoSi_2$ grains at high temperature, limits the material's resistance to creep [11, 31]. Another factor affecting the creep is grain size. Usually, the creep rate is related to the grain size as $\sqrt{d^{-3}}$ for Coble creep (grain boundary diffusion) or $\sqrt{d^{-2}}$ in case of Nabaro-Herring creep (bulk diffusion) [32]. For dislocation creep (Power law), which is the main creep process at high stresses, the creep rate is normally not affected by the grain size. However, in case of $MoSi_2$, the creep rates at both the diffusion and the dislocation regimes are very sensitive to the grain size, indicated by a grain size exponent much larger than the suggested ones [11, 31, 33, 34]. Sadananda *et al.* [33, 34] have investigated the creep behaviour at 1200 °C and found that the grain size exponent was about 4.3 for all creep regimes.

Another mechanism leading to softening of metals and alloys is dynamic recrystallisation, in which defect-free grains nucleate and grow [35, 36]. In case of $MoSi_2$, dynamic recrystallisation has been reported by some researchers, [37] but was not observed by Mitra *et al.* [31]. Hardwick *et al.* [37] showed that dynamic recrystallisation of $MoSi_2$ was very temperature and strain rate dependent, the phenomenon was only observed in specimens being compressed to high strain (57 %), using a strain rate of $1 \cdot 10^{-4}$ s^{-1} at 1300°C.

In order to improve the high-temperature strength and creep resistance of $MoSi_2$, C or Al can be added to reduce the amount of SiO_2, which prevents grain boundary sliding, by forming SiC and Al_2O_3, respectively [11]. In case of the $MoSi_2$-SiC material, it is important to add a sufficient amount of C, since SiC also acts as grain refiner [31, 34]. As has been discussed above, the creep rate is higher for a fine-grained material due to the high grain size exponent, hence, a certain amount of SiC needs to be added in order to overcome this effect and improve the creep resistance. It has been shown that 2 wt.% C addition gives a microstructure with 30-40 vol.% SiC, which is necessary to obtain a material with an improved creep resistance [11].

2.4.2 $Mo(Si,Al)_2$

If alloying $MoSi_2$ with Al, it is important to keep the Al content low. If the Al addition is high enough to stabilise the hexagonal C40 structure, the creep rate is higher than that of $C11_b$ structured material. The higher creep rate of C40 has been shown in single crystals and in multi-phase material containing both $C11_b$ structured $MoSi_2$ and C40 structured $Mo(Si,Al)_2$ [11, 15, 23] phases.

The deformation behavior of single crystalline C40 structured $Mo(Si,Al)_2$ has been studied by Inui *et al.* [26, 38, 39]. In one study [26], the plastic deformation of single crystalline $Mo(Si,Al)_2$, having different orientations and Al

contents ($Mo(Si_{1-x}Al_x)_2$, x=0.15 and x=0.2 respectively), was investigated in compression at temperatures up to 1500 °C. Samples oriented with the [0001] or $[1\bar{2}10]$ direction along the compression axis did not deform at all, while $[1\bar{2}12]$ and $[1\bar{2}11]$ oriented crystals were deformed by basal (0001) slip with Burgers vectors of $\frac{1}{3}[1\bar{2}10]$ and $\frac{1}{3}[11\bar{2}0]$. The DBTT of $Mo(Si_{0.85}Al_{0.15})_2$, was reported to 1100°C and the yield stress decreased with increasing temperature, see Figure 2.5(a).The higher Al-alloyed $Mo(Si_{0.80}Al_{0.20})_2$ had a higher DBTT than $Mo(Si_{0.85}Al_{0.15})_2$ (Figure 2.5(b)). In Figure 2.6 typical stress-strain curves from compression at different temperatures are shown.

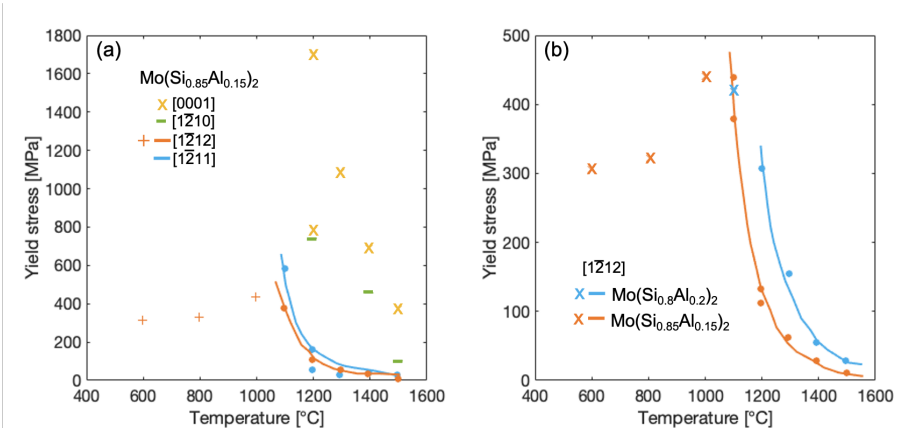

Figure 2.5: Yield stress as a function of temperature of (a) four different orientations of $Mo(Si_{0.85},Al_{0.15})_2$ single crystal, (b) $[1\bar{2}12]$ oriented $Mo(Si_{0.85},Al_{0.15})_2$ and $(Mo(Si_{0.80},Al_{0.20})_2$ single crystals. X, - and + indicate stress at fracture. The figures are based on data from [26]

The CRSS of $[0001]\langle 1\bar{2}10\rangle$ slip system in $Mo(Si,Al)_2$ was calculated and compared with that of the $\{110\}\langle 111]$ slip system in single crystalline $C11_b$ $MoSi_2$ [26] (remember: the stacking sequence of thees atomic planes are the same: ABCABC). The At elevated temperature, the CRSS of $Mo(Si_{0.8},Al_{0.2})_2$ is very similar to values obtained from $MoSi_2$, see Figure 2.7. Also shown in the figure is the anomalous increase of CRSS in case of $MoSi_2$, but not in $Mo(Si,Al)_2$.

$[0001]\langle 1\bar{2}10\rangle$ is the only slip system active in the C40 structure [11, 26, 38, 39]. In Inui *et al.*'s study [26] $\frac{1}{3}[1\bar{2}10]$ was the dominating dislocation type. This dislocation dissociates into two synchro-partials with identical Burgers vector ($\frac{1}{6}[1\bar{2}10]$, from now on referred to as $\mathbf{b}_1$), with a stacking fault in between. The synchro-partials further dissociate into two additional partials on adjacent atomic planes, leading to synchronous shearing of the crystal. Figure 2.8 shows how such a partial shearing could take place in order to achieve the total displacement of one of the synchro-partials with the Burgers vector $\mathbf{b}_1$[26]. The Burgers vectors are indicated in Figure 2.9.

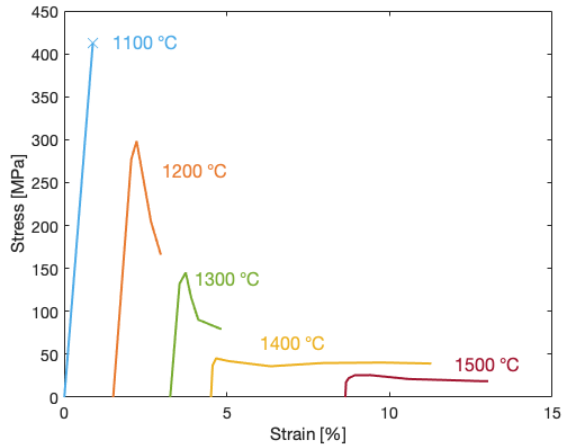

Figure 2.6: Stress strain curves obtained from a $[1\bar{2}12]$ oriented $Mo(Si_{0.80}Al_{0.20})_2$ single crystal tested in compression at elevated temperatures. Based on data from [26]

The original stacking sequence of atomic layers parallel to the basal planes is shown on the left-hand side in Figure 2.8. A layer (called Layer 1) containing atoms positioned at A sites, is displaced by -$\mathbf{b}_2$. The adjacent Layer 2 with atoms at B positions, as well as all layers above this layer, are displaced by the same vector. At the same time, Layer 2, and all the above layers, are further displaced by -$\mathbf{b}_3$. The resulting sequence is shown on the right-hand side of the figure. The total displacement of Layer 2, and all layers above, is $\mathbf{b}_1$ ($\mathbf{b}_1$ = -$\mathbf{b}_3$-$\mathbf{b}_2$). The first synchro-partial is followed by an identical, trailing, synchro-partial, containing exactly the same partials. Figure 2.10(a) shows all partials in the leading and trailing synchro-partial. As can be seen on the left-hand side of the figure, the total shear of Layer 2 is $2\mathbf{b}_1$, which equals $\frac{1}{3}[1\bar{2}10]$, the Burgers vector for the full dislocation.

Inui *et al.* [26] also studied the dislocation core using High-Resolution Transmission Electron Microscopy (HRTEM), and found that the total displacement of Layer 1 suggested by the model in Figure 2.10(a) was not in line with HRTEM results. Therefore, an alternative model, shown in Figure 2.10(b), was suggested. Even though this model does not show the unexpected displacement of Layer 1, it has other drawbacks compared to the former model. The two synchro-partials are not symmetrical, and the Burgers vector of one of the partials is rather complicated and may disintegrate into three new partials. Therefore, it is more likely that the former model best describes the deformation of $Mo(Si,Al)_2$ with C40 structure, even though the displacement of Layer 1 is not in line with the TEM observations. A theory, but not yet verified, is that diffusion of Al may be a part of the full explanation [26].

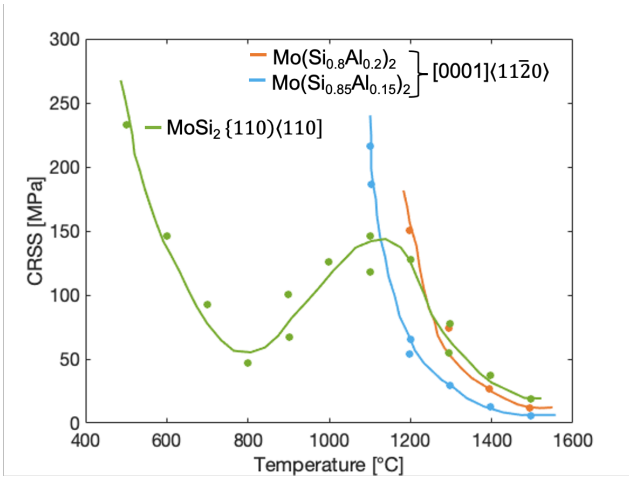

Figure 2.7: CRSS as a function of temperature of single crystalline $Mo(Si,Al)_2$ and $MoSi_2$. The figure is based on data from [26]

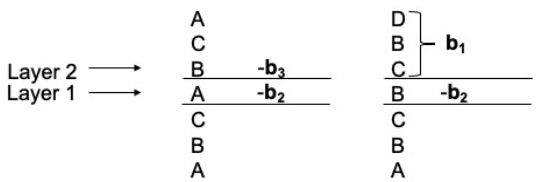

Figure 2.8: Synchroshear mechanism giving rise to a total displacement of $\mathbf{b}_1$ of Layer 2 and all layers above.

The research on polycrystalline $Mo(Si,Al)_2$ is very limited. A DBTT of 1250 °C for a material consisting of 100 vol.% $Mo(Si,Al)_2$ has been reported by Hagihara *et al.* [40, 41], who also shown that the yield stress decreases rapidly as the temperature increases, see Figure 2.11. Also shown in Figure 2.11 is the 0.2 % yield stress of the two $MoSi_2$ polycrystalline materials studied by Mitra *et al.* [31]. The yield stresses reported of the materials are close. However, the definition used for the yield stress, as well as the grain size in the case of $Mo(Si,al)_2$ is unknown, and no stress-strain curves or microstructure investigations were reported by Hagihara *et al.* In order to understand the deformation behavior of polycrystalline $Mo(Si,Al)_2$, further investigations are needed.

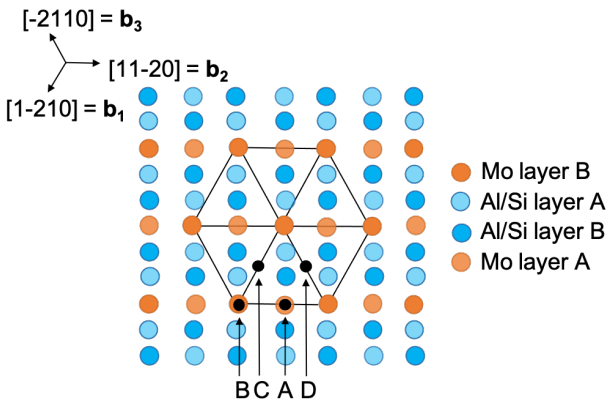

Figure 2.9: stacking of C40 basal layers. The bright atoms are positioned in Layer B, positioned above Layer 1 (faded atoms). Position A, B, C and D indicate possible sites for Mo atoms in layers positioned above Layer B. The possible Burgers vectors for a glide along the basal plane is shown in the top left corner

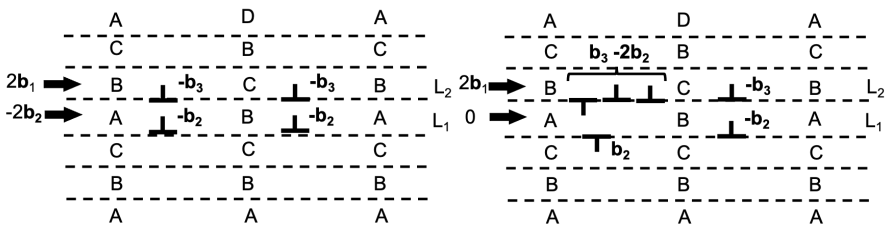

Figure 2.10: Two models of synchro-shear mechanisms giving rise to the total displacement of $\mathbf{b}_1$ of L_2 and the layer above

2.4.3 Other C40 structured silicides

As mentioned in the previous section, $Mo(Si,Al)_2$ deforms plastically due to the synchro-shear mechanism. Another C40 structured silicide deforming by the same mechanism is $CrSi_2$ [12, 41–43]. However, other C40 structured silicides, VSi_2, $TaSi_2$ and $NbSi_2$, deform in a more conventional manner, similar to the deformation of $C11_b$ structured $MoSi_2$ [12, 41–43]. The two mechanisms affect the mechanical properties if the materials, e.g. single crystalline VSi_2, $TaSi_2$ and $NbSi_2$ can be deformed at room temperature, [11, 43–45], while the onset of plastic flow for $Mo(Si,Al)_2$ and $CrSi_2$ is much higher, 1100°C and 700 °C, respectively [39], see Figure 2.12, which corresponds to an onset temperature of 0.6 T/T_m (T_m: melting temperature). In case of VSi_2, $TaSi_2$ and $NbSi_2$, the onset is found close to 0.3 T/T_m. Furthermore, the silicides having the

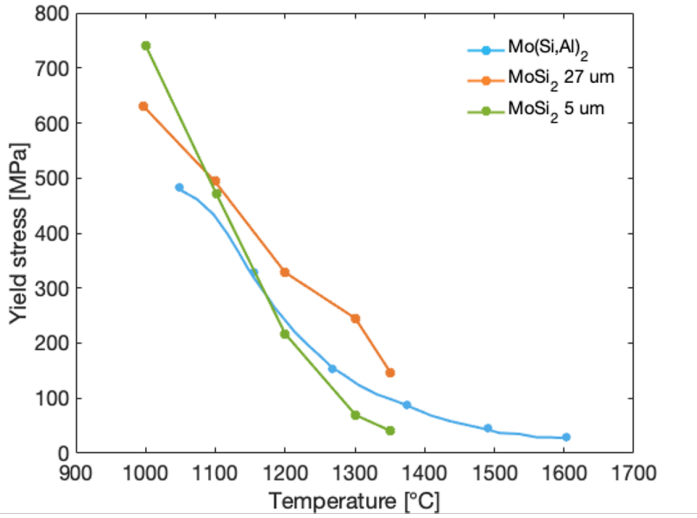

Figure 2.11: Temperature dependence of yield stress in polycrystalline $Mo(Si,Al)_2$ and $MoSi_2$ (grain size = 5 μm and 27 μm). The figure is based on data from [41] and [31]

lower onset temperature also shown an anomalous increase of the yield stress [11, 43–45], (Figure 2.12). This has not been observed in either $Mo(Si,Al)_2$ or $CrSi_2$ [26, 43].

In a recent study, Kishida *et al.* [46] investigated the deformation behaviour of single crystals of C40 structured disilicides at low temperature using micropillar compression. Interestingly, even $CrSi_2$ deformed plastically when tested at the microscale, slip occurred through conventional shear at room temperature, but changed to synchroshear at 700 °C [46].

Traditionally all C40 structured silicides are said to be deformed by only only slip system, $[0001]\langle 1\bar{2}10\rangle$ [11, 43–45]. However, when a $NbSi_2$ single crystal was tested in tension at elevated temperature, four additional slip systems ($\langle 1\bar{2}10\rangle\{10\bar{1}0\}$, $\langle 1\bar{2}10\rangle\{10\bar{1}1\}$, $\langle 0001\rangle\{10\bar{1}0\}$ and $\langle 11\bar{2}X\rangle\{11\bar{2}Y\}$, where (X×Y) = -6) were found to be operative in the vicinity of crack path to accommodation of local stress concentration [44].

The deformation mechanisms of all C40 structured silicides, both the binary silicides presented in this section, and the ternary $Mo(Si,Al)_2$ discussed in the previous section, need to be studied more in detail in order to be fully understood. Due to the different deformation mechanisms it would also be of interest to study quaternary systems, e.i. alloying $Mo(Si,Al)_2$ with e.g. Nb or Ta, which show anomalous increase in yield stress at high temperatures.

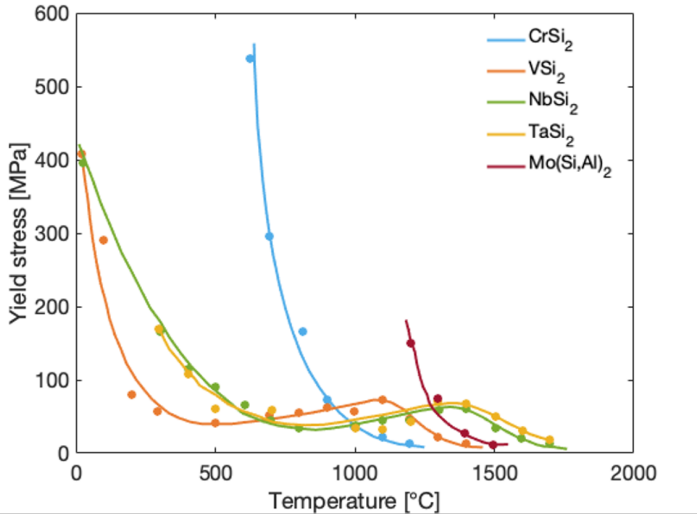

Figure 2.12: Temperature dependence of yield stress in various C40 single crystals. Based on data from [41] and [26]

2.5 Oxidation of silicides

Good mechanical properties are not the only requirements for a high-temperature material. In addition, the material must be corrosion resistant. One way to achieve this is to coat the material with a corrosion-protective coating. However, for some materials, this is not needed, due to their inherent ability to form protective oxide scales on the surface when in contact with oxygen. Once a covering scale is formed, oxygen can not reach the bulk material. Thus, the material is protected from further oxidation. If the scale fails to protect the material, the oxidation process will continue, leading to depletion and failure of the material.

Many silicides (e.g. $MoSi_2$ and WSi_2) form protective SiO_2 scales when exposed at high temperature. In case of $Mo(Si,Al)_2$, Al_2O_3 will be formed due to the higher oxygen affinity of Al than that of Si. As will be discussed in the following sections, oxidation behaviour is highly dependent on the temperature.

2.5.1 $MoSi_2$

$MoSi_2$ is a silicide with excellent corrosion resistance at high temperature due to the formation of a protective and fully covering glassy SiO_2 scale [47–50]. However, at intermediate temperatures (400-700 °C), the material suffers from accelerated oxidation and may disintegrate to a powder. This phenomenon, called pesting, was first described by Fitzer 1955 [19, 51–53]. In oxygen containing environment, both Si and Mo oxidise as shown in the following reaction

$$2MoSi_2 + 7O_2 \rightarrow 2MoO_3 + 4SiO_2$$

The volume expansion attributed to the oxide formation at grain boundaries introduces stresses, leading to that cracks can easily propagate and pulverise the material [19, 53].

The above oxidation process also takes place in the initial stage of oxidation at high temperatures. Due to the high vapour pressure of MoO_3 at elevated temperature, the formed MoO_3 evaporates immediately [11]. In addition, the SiO_2 scale on the surface effectively decreases the oxygen partial pressure at the oxide/material interface, and the oxidation rate decreases. Above 1700 °C, the viscosity of the glassy SiO_2 scale decreases, and the oxidation decreases due to an increase in defect concentration [11].

2.5.2 $Mo(Si,Al)_2$

Alloying $MoSi_2$ with Al effectively suppresses the pesting at intermediate temperatures. The oxygen affinity of Al is higher than that of both Si and Mo, leading to the formation of a Al_2O_3 scale on the surface. Another advantage of the alumina-former is that it can be used in both oxidising and reducing atmospheres. However, the maximum working temperature in air (1580 °C) is somewhat lower than that of $MoSi_2$ [7, 18]. The oxidation of $Mo(Si,Al)_2$ has been studied by a few research groups [18–21, 23, 51, 52, 54, 55]. One of the most extensive works has been done by Ingemarsson *et al.*, who studied the oxidation of the $Mo(Si,Al)_2$ material "Kanthal Super ER" at the temperature range of 300-1600 °C [18–21]. Both the chemical composition and the volume fractions of $Mo(Si,Al)_2$, $Mo_5(Si,Al)_3$ and Al_2O_3 of Kanthal Super ER are similar to the materials used in the work presented in this Licentiate Thesis. Therefore, the work by Ingemarsson *et al.* is of particular importance and will be presented more thoroughly.

In one study, Ingemarsson *et al.* studied the oxidation of $Mo(Si,Al)_2$ at intermediate temperatures (300-1000 °C) [19]. It was shown that $Mo(Si,Al)_2$ formed a mixed oxide scale consisting of both Al_2O_3, SiO_2 and MoO_3. Worth

mentioning is that the composition of the oxide scale differed spatially due to the multi-phase character of the $Mo(Si,Al)_2$ material used. The covering "base oxide" consisted of a mixture of oxidised Al, Si and Mo, but at some places, probably on top of $Mo_5(Si,Al)_3$ grains, flake-like MoO_3 and SiO_2 protrusions were present. Pure MoO_3 crystals were also observed on the surface. The mass gain (due to oxygen uptake) increased with increasing temperature up to 500 °C, see Figure 2.13. At 600-700 °C, the mass gain initially increased with oxidation time. After some time, MoO_3 started to evaporate, leading to mass loss. No MoO_3 crystals were found on the surface after long oxidation times. Also, the Mo content of the base oxide decreased with increasing oxidation time and temperature. However, the thickness of the base oxide increased with increasing temperature, and, thus, the total mass gain (after 72 h oxidation) increased at temperatures above 600 °C, see Figure 2.14. At 1000 °C, the scale consisted of relatively pure Al_2O_3, and only small amounts of SiO_2 were detected [20]. Furthermore, no disintegration (pesting) of the substrate was observed within the accelerated oxidation regime.

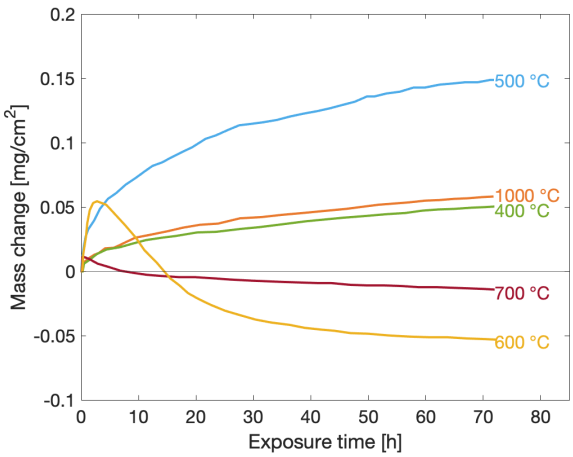

Figure 2.13: The mass changes as a function of exposure time for the $Mo(Al,Si)_2$-based material exposed in synthetic air at different temperatures. Based on data from [20]

At temperatures above 1000 °C, $Mo(Si,Al)_2$ forms dense and protective Al_2O_3 scales [18, 21, 56]. The oxidation rate increases with increasing temperature, and the mass gain is higher than that of $MoSi_2$, see Figure 2.15.

At the oxide/$Mo(Si,Al)_2$ interface, a $Mo_5(Si,Al)_3$ layer is present. The thickness of this layer is approximately the same as the oxide. Ingemarsson *et al.* [56] have proposed the following simplified formula describing the overall

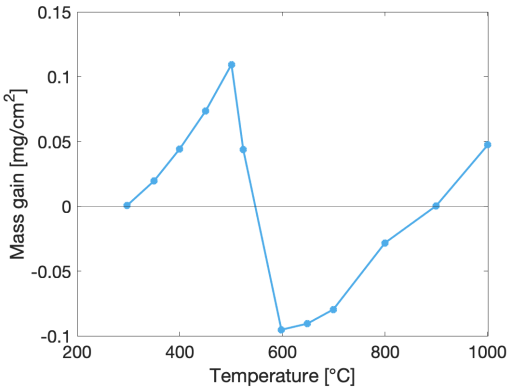

Figure 2.14: The mass changes of a $Mo(Si,Al)_2$-based material that was exposed at 300–1000 °C for 72 h in dry synthetic air. Based on data from [20]

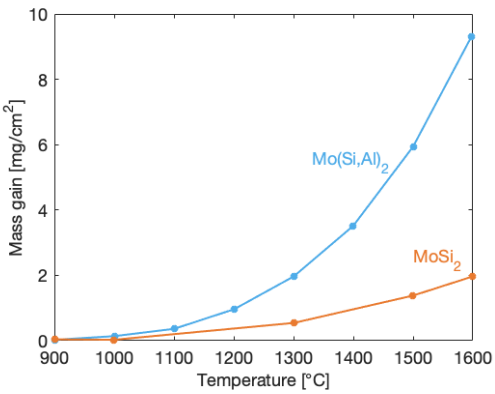

Figure 2.15: Mass gain of $Mo(Si,Al)_2$ and $MoSi_2$ after 72 h oxidation as a function of temperature. Based on data from [18]

oxidation process

$$(25x + 10)\ \mathrm{MoSiAl} + 10.5\ x/4\ \mathrm{O_2} \rightarrow$$
$$35x/2\ \mathrm{Al_2O_3} + 10\ \mathrm{Mo(Si_{1+x},Al_{1-x})} + 5x\ \mathrm{Mo_5Si_3}$$

The Mo:Si:Al atomic ratio of the material used was close to 1:1:1, why MoSiAl rather than $Mo(Si,Al)_2$ is used in the formula. The Al content of $Mo_5(Si,Al)_3$ layer was very low, thus, this phase is written as Mo_5Si_3. The decrease in volume attributed to the phase transformation of $Mo(Si,Al)_2$ to $Mo_5(Si,Al)_3$, leads to a porous Mo_5Si_3 layer [56]. The layer also contains Al_2O_3 grains, encapsulated by the inwards growth of the $Mo_5(Si,Al)_3$ layer, see Figure 2.16.

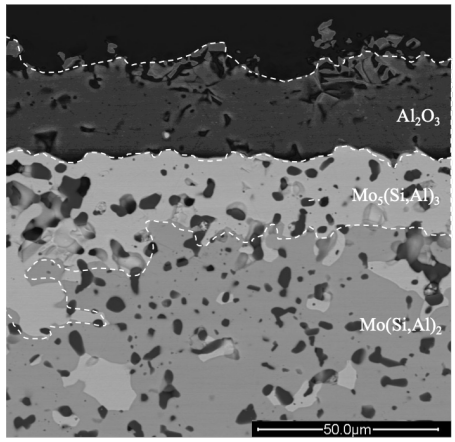

Figure 2.16: BSE cross section image of $Mo(Si,Al)_2$ after oxidation. Between the oxide scale (Al_2O_3) and the bulk material, the $Mo_5(Si,Al)_3$ layer can be seen

Due to preferential oxidation, an Al gradient was found in the $Mo(Si,Al)_2$ below the $Mo_5(Si,Al)_3$ layer. Immediately beneath the $Mo_5(Si,Al)_3$ layer, the Al content was low, but it increased gradually to the bulk concentration deeper in the material. A similar, but with opposite sign, gradient of Si was present to keep the $Mo(Si,Al)_2$ stoichiometry [56].

In one study [56], the oxide formed on $Mo(Si,Al)_2$ oxidised at 1500 °C was studied more in detail. It was shown that the inner part of the oxide consisted of elongated grains, while the outer part consisted of a mix of equiaxed Al_2O_3 grains and Na-Si-Al-O glass when exposed for 162 h. Na is believed to originate from the material synthesis, which involves the element found. After longer oxidation times, no glass, but mullite ($3Al_2O_3{\cdot}2SiO_2$) and SiO_2, were found in the outer part of the oxide. It is believed that Na_2O evaporates with time and that the glass is replaced by mullite and SiO_2 [56].

At elevated temperatures, where the material forms a protective alumina scale, spallation of the oxide scale is very low [56]. However, internal reports at Kanthal have communicated that spallation may occur, especially if the diameter of the element is relatively large. As explained in the introduction of this thesis, there is a strive to manufacture heating elements in the MW scale. To achieve this, elements having larger diameters are probably required, hence, it is important to make sure that oxide adhesion is not affected by the increase in size.

CHAPTER 3

Synthesis of materials and experimental methods

3.1 Material synthesis

Polycrystalline $Mo(Si,Al)_2$ material can be manufactured by a number of synthesis routes. For the projects presented in this thesis, two types of materials have been produced and investigated, unalloyed $Mo(Si,Al)_2$ for a deformation study, and Y-alloyed $Mo(Si,Al)_2$ for an oxidation study. In the following section, the process used to produce the unalloyed material will be described. The synthesis of the Y-alloyed materials will be commented at end of this section.

The process started by the mixing of elemental powders, Mo (99.9 % purity, Cerac Inc.), Si (99.99 % purity, Wacker) and Al (99.5 % purity, GoodFellow). The powder ratio was chosen to obtain a material with similar chemical composition as Kanthal Super ER. A cylinder made of Mo metal sheet was filled with the well-mixed powder and placed in a tube furnace with Ar gas flow. The furnace was heated at a rate of around 70 °C min^{-1}, and when the temperature reached 820 °C, the powder ignited and a self-propagating reaction was started. Due to the exothermic behaviour, the course of reaction could easily be followed, see Figure 3.1. When all powder had reacted, the furnace was turned off and the reaction product (shown in Figure 3.1(c)) was left cooling in the Ar flow.

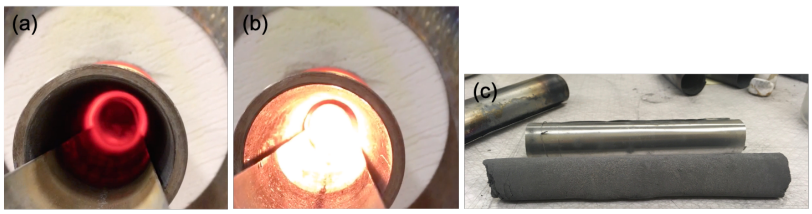

Figure 3.1: Powder filled Mo cylinder in a tube furnace, (a) prior reaction, (b) at the moment of reaction, (c) the reaction product and the Mo metal sheet cylinder

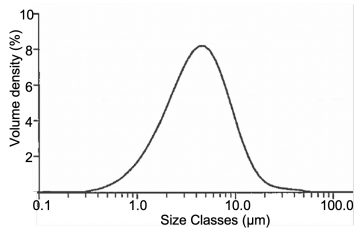

Figure 3.2: Particle size distribution of milled powder

The reacted material was milled in a Mo-lined vial container with gasoline and Mo balls for 228 h. The final powder had a surface area of 1.88 m^2/g. The particle size distribution is shown in Figure 3.2.

After milling, the powder was dried and prepared for sintering. This was done by filling soft rubber moulds with powder, see Figure 3.3(a). The powder was compacted to green bodies using a cold isostatic press (CIP), operating at 2000 bar. The green bodies were sintered in H_2 gas at 1650 °C for one hour. The green bodies and the sintered material are shown in Figure 3.3(b) and (c), respectively.

The Y-alloyed materials were produced by Kanthal AB in a similar way, but the exact processing conditions are not known. Detailed microstructure analysis of the different materials is presented in Section 4.1.

3.2 Experimental methods

The research work presented in this thesis can be divided into two parts: a) oxidation of yttrium alloyed $Mo(Si,Al)_2$ based material and b) high-temperature compression of $Mo(Si,Al)_2$. The two methods will be described in the following sections.

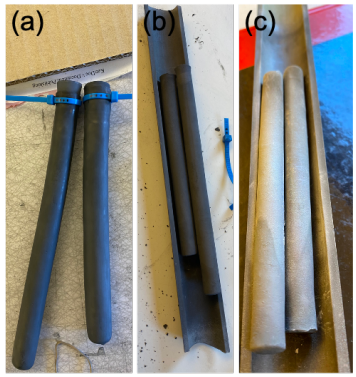

Figure 3.3: (a) Rubber mould filled with powder, (b) green bodies after CIP, (c) sintered material

3.2.1 Oxidation

For the oxidation study, the as-sintered material was ground with 500 mesh SiC paper to remove the surface layer prior to cutting into circular samples. Three identical samples of each composition were prepared and placed in a box furnace, which was heated to 1500 °C using a ramp time of 5 h. After 24 h at the target temperature the furnace was turned off. When the temperature was about or below 200 °C, the furnace was opened and one sample of each composition was removed for microstructure analysis. Furthermore, one samples of each composition was weighted and put back in the furnace in order to measure mass gain. The furnace was again heated to 1500 °C. After additional 26 h (a total exposure time of 50 h) the procedure was repeated. After another 200 h (a total exposure time of 250 h), the remaining samples were taken out. The procedure, resulting in materials being oxidised for 24, 50 and 250 h, is shown in Figure 3.4.

3.2.2 Compression

A number of test methods can be used to evaluate the mechanical properties of a material. For example, the fracture toughness can be measured from an indentation test and the tensile strength can be determined from a tensile test. The tensile test is very common in the case of metals and alloys, but due to a number of reasons, ceramic materials are not often tested using this method. Ceramic materials are seldom perfectly dense, but contains a lot of pores. Such defects make it challenging to produce the test specimen. Furthermore, if the system is not perfectly aligned, the ceramic specimen will probably fracture

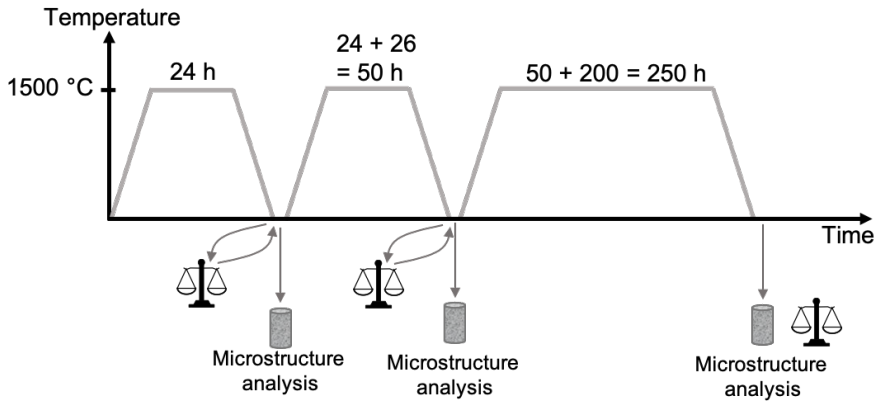

Figure 3.4: Schematic illustration of the oxidation cycle

because of its very low fracture toughness. The compressive fracture strength of ceramics is generally much greater and, hence, easier to measure, than the tensile fracture strength [32]. Therefore, the $Mo(Si,Al)_2$ material in this PhD thesis has been tested in compression. Another common testing method for ceramics is the four-point bending test, in which the material is subjected to both compressive and tensile stresses. This type of test will be carried out at a later stage of this project.

Since the long term goal of this project is to understand and improve the high-temperature mechanical properties of $Mo(Si,Al)_2$ based materials, it is of course very important to test the material at high temperature. In this project, we have used a Gleeble system (Gleeble 3800 thermomechanical simulator [57]) in order to test the material. In addition to testing the compressive and tensile strength of a specimen, the Gleeble system can also be used to simulate a number of difficult and demanding metallurgical processes e.g. welding, forging, annealing, quenching and casting. Such experiments require very high temperatures and high heating and cooling rates. The system used in this thesis had a maximum temperature of 3000 °C and heating and cooling rates of up to 10 000 °C s^{-1} [57]. The tested specimen is heated by resistivity heating, and the temperature is often controlled using thermocouples. When it comes to the mechanical system, the hydraulic servo system allows for both high (2 000 mm s^{-1}) and low (0.001 mm s^{-1}) displacement rates. In compressive testings, the force can be up to 20 kN [57].

In this project polycrystalline $Mo(Si,Al)_2$ was tested at a temperature of 1300-1400 °C and a strain rate of $1 \cdot 10^{-4}$ s^{-1}. The selected temperature and strain rate are relevant for both the final application of the $Mo(Si,Al)_2$, and allow for comparison with literature. The specimens were prepared by grinding and

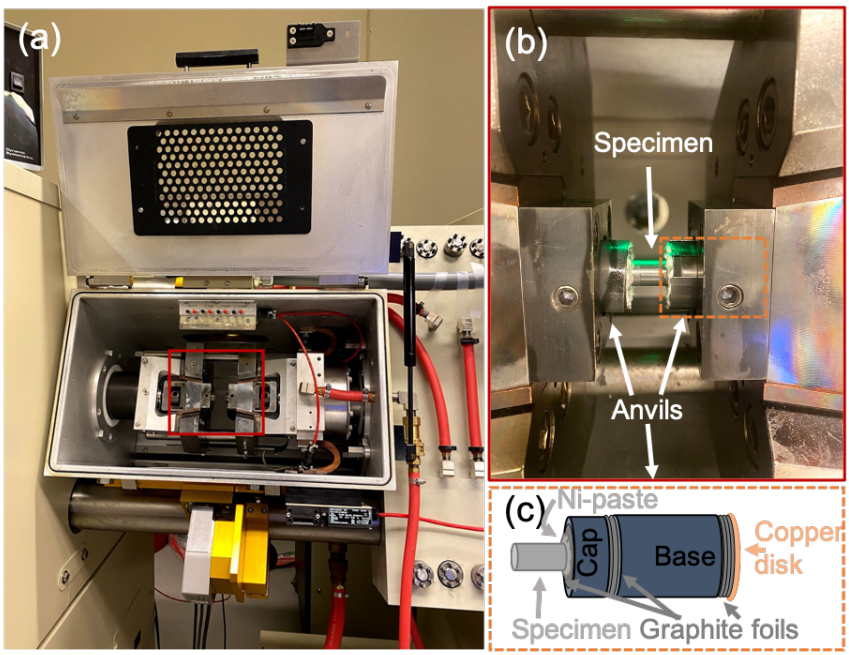

Figure 3.5: (a)The Gleeble system used for compression (b) close up of the specimen placed between the anvils, (c) schematic figure showing the specimen and one of the ISO-T anvils

cutting the sintered $Mo(Si,Al)_2$ material to cylindrical specimens having a diameter of 8 mm and a height of 12 mm.

In Figure 3.5(a) a photo of the Gleeble apparatus is shown. The specimen is placed in the gap between two anvils, see Figure 3.5(b). Ni-paste and graphite foils are placed between the specimen and the anvils in order to ensure electrical contact. The anvils used in this project are so-called ISO-T anvils, designed to keep a constant and even temperature of the test specimen. The anvils are built up by two cylindrical hard metal (WC-Co) parts, a cap and a base, with graphite-foils in between, see Figure 3.5(c). The anvils are held in place by two jaws. The jaw on the left-hand side of the specimen in Figure 3.5(a)) is connected to the hydraulic servo system and can be moved back and forth, while the jaw on the other side of the specimen is static.

Two different systems can be used to measure the displacement of the specimen. The first system is the stroke, which was used to control the compression. The other system, called L-Gauge, is a secondary system measuring the displacement of the jaws. The stroke and L-Gauge displacements differ to some extent, the stroke measures the displacement further away from the test spec-

imen and is to a larger extent influenced by the compliance of the different parts of the apparatus. The compliance of the jaws, the anvils, the Ni-paste and the graphite foil (see Figure 3.5(c)) does however to some extent also affect the displacement measured by the L-Gauge. It might be tempting to use the L-Gauge to control the compression, but due to the rather slow response time between the L-Gauge and the hydraulic system, using this system results in an uneven compression rate. Therefore, the stroke was used to control the compression. Due to the higher accuracy of the L-gauge, this system was used to generate the stress-strain curves.

As mentioned, the temperature is often controlled by thermocouples, which are welded to the surface or inserted in holes drilled in the specimen. However, none of these options was possible when testing the ceramic $Mo(Si,Al)_2$ material. It is not possible to weld the thermocouples to the non-metallic surface, and the brittle behaviour makes drilling in the specimen very challenging. Attempts were made to attach the thermocouples using high-temperature ceramic paste. This alternative failed for a number of reasons. Firstly, it could not be guaranteed that the temperature measured actually was the temperature of the specimen. If the Gleeble system was controlled by a temperature measured within the much cooler paste, the temperature of the specimen itself would have been much higher than the wanted temperature. In one test, where a steel specimen was used for testing the ceramic paste alternative, it was shown that the temperature measured by thermocouples attached with the paste showed a temperature of about 120 °C lower than the temperature measured by thermocouples welded to the surface. Furthermore, even if it would have been possible to measure the surface temperature, the ceramic paste would have fractured and fallen off when the compression started.

Instead of using thermocouples for the control and measurement of the temperature, a pyrometer, which measures the thermal radiation emitted from a surface, was used. If the surface changes e.g. due to oxide formation, the radiation changes as well. It was shown that even if the $Mo(Si,Al)_2$ material was heated to elevated temperatures in (low) vacuum, the material oxidised to some extent, which affected the temperature read by the pyrometer. This problem was solved by wrapping a thin, flexible graphite foil around the test specimen, see Figure 3.6. The surface of the graphite foil was not affected

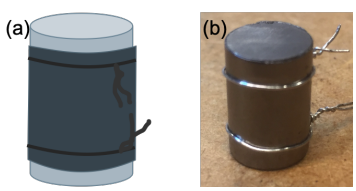

Figure 3.6: (a) schematic figure, (b) photo of the test specimen with graphite foil

by the high temperature. The system was calibrated using steel specimens, to which also a thermocouple was welded. The temperature was adjusted in steps up to 1100 °C, and the temperature read by the pyrometer was compared with the thermocouple. The temperature measured by thermocouple and pyrometer agreed to ± 10 °C, and the emissivity measured by the pyrometer did not change with time.

For higher temperatures, at which the steel specimen could not be used, the reliability of the system was confirmed using a polycrystalline $MoSi_2$ material. The $MoSi_2$ specimen was tested in compression at a temperature of 1300 °C and a strain rate of $1{\cdot}10^{-4}$ s^{-1}. The resulting stress-strain behaviour was compared with literature values of similar material [31].

The $MoSi_2$ material was also tested at 1400 °C. Unfortunately this temperature was too high for the anvils, which were deformed along with the specimen. Therefore, it was decided to use a temperature of 1300 °C for the final tests of $Mo(Si,Al)_2$. At 1300 °C, the anvils were not deformed significantly.

When the method was validated, a program for testing the $Mo(Si,Al)_2$ specimens was written. The first step of the program was to apply a compressive force of 0.4 kN in order to make sure that the sample was kept in place. The pyrometer can not be used at too low temperatures, therefore, the initial heating was done using a constant power supply. When the temperature reached 450 °C, the pyrometer could be used for temperature control. A heating rate of 50 °C min^{-1} was used to heat the specimen up to the target temperature of 1300 °C. When the temperature was reached, the specimen was held for temperature stabilisation for 30 s prior to compression.

3.3 Microstructure analysis

The microstructure of both as-sintered material and deformed and oxidised materials was studied using several techniques: X-ray diffraction (XRD) was used for phase identification, scanning electron microscopy (SEM) based methods for imaging (secondary electrons (SE) and backscattered electrons (BSE)), chemical composition (Energy Dispersive X-ray Spectroscopy (EDS)) and crystal structure (Electron Backscatter Diffraction (EBSD)). In the following sections, the use and the advantages of the different methods are presented. The basics of the different methods will not be covered.

3.3.1 X-ray diffraction

X-ray Diffraction (XRD) is a very useful tool when working with crystalline materials. X-rays are produced from the interaction of electrons (accelerated from a tungsten filament) with and a metal (often Cu or Mo). The interaction gives rise to a continuous X-ray spectrum, which is filtered to obtain a monochromatic X-ray beam. The beam is then focused on the sample at an incident angle θ, see Figure 3.7. If the Bragg's law,

$$n\lambda = 2d_{hkl}\sin(\theta_{hkl}) \tag{3.1}$$

where n is an integer and d the interplanar spacing, is fulfilled, the diffracted X-rays give rise to peaks in the XRD pattern. In reality, the diffraction is more complex, the curious reader is referred to textbooks (e.g. "X-ray Diffraction - A Practical Approach" by C. Suryanarayana and M. Grant Norton [58]) for deeper understanding.

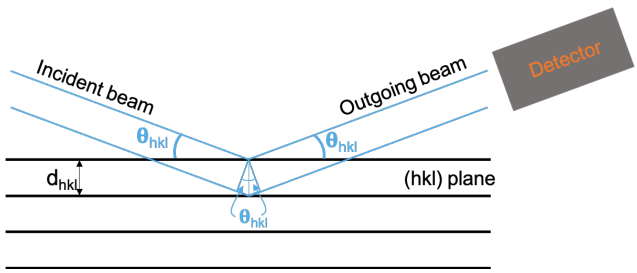

Figure 3.7: The Incident X-ray beam is diffracted by the (hkl)-planes. The incident angle is θ and the d is the interplanar spacing

The position of the Bragg peaks in the XRD pattern can be used for phase identification, see Figure 3.8. In this work, XRD was used to obtain information about the crystal structure (i.e. phase identification) and not the chemistry. Therefore, XRD was combined with other methods, such as EDS, in order to fully characterise the materials.

3.3.2 Scanning electron microscopy

The main part of the microstructure analysis conducted in this work was done using SEM based methods. The generation of electron beam, and other basics of SEM, is presented elsewhere, e.g. in the book "Scanning Electron Microscopy and X-Ray Microanalysis" by J. Goldstein *et al.* [59].

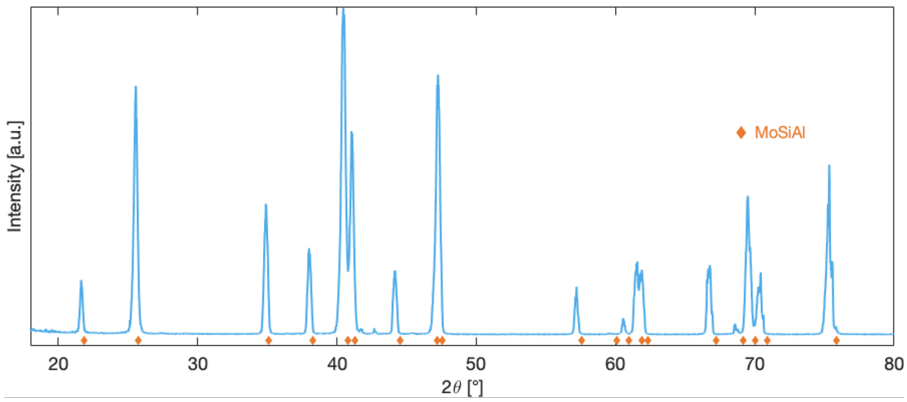

Figure 3.8: XRD pattern of a $Mo(Si,Al)_2$ material. The slight shift in 2θ is due to small differences in chemical composition of the material analysed and the material which the XRD card was based on (PDF 00-057-0374)

Imaging

In SEM, the sample of interest is scanned by an electron beam. The interaction gives rise to two different types of scattered electrons, Secondary electrons (SE) and Backscattered Electrons (BSE) [59]. From the secondary electrons, which are generated from a sample depth of just a few nm, an image showing topographic contrast can be obtained. In this work, SE images have mainly been used to study the porosity of the materials. In Figure 3.9(a) the pores in a $Mo(Si,Al)_2$ based material are clearly visible due to the dark contrast and bright edges.

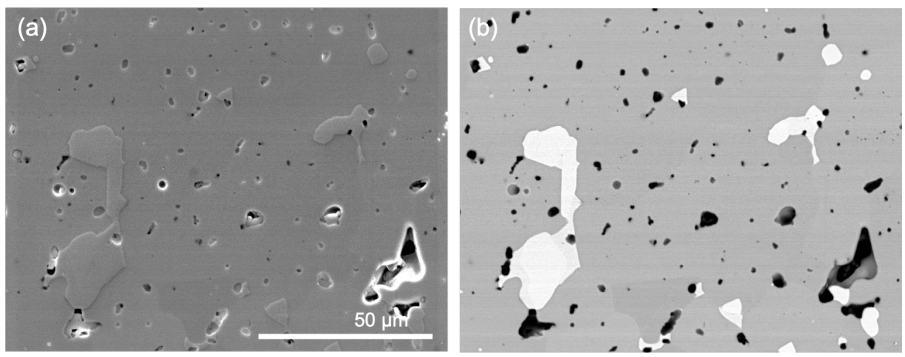

Figure 3.9: Two types of SEM images captured using (a) secondary electron, (b) backscattered Electrons

The BSE image of the same area is shown in Figure 3.9(b). The depth from

which the backscattered electrons are generated is somewhat larger than that of SE [59]. The contrast is related to the atomic number of the element present in the area analysed. Heavy elements scatter more, therefore they give rise to a higher signal and a bright contrast in the image. Light elements appear darker [59]. In Figure 3.9(b), three different phases can be seen, the brightest grains are $Mo_5(Si,Al)_3$, the grey phase is $Mo(Si,Al)_2$ and the dark grains are Al_2O_3. However, it is difficult distinguishing between pores (dark due to no signal) and Al_2O_3 (dark due to low average atomic number). Therefore, the two types of images have often been combined (using GIMP [60], a digital image editing software) when calculating the volume fraction of phases and pores.

Energy dispersive X-ray spectroscopy

The chemical composition of the phases was measured using EDS. In addition to scattering of electrons, the electron beam/sample interaction gives rise to characteristic X-rays [59]. The X-rays are detected and the chemical composition can be calculated from the energy spectrum, see Figure 3.10 [59]. If the electron beam is scanned over the sample surface, maps showing the occurrence of different elements can be created. The X-rays are generated from a larger volume of the sample, hence, the resolution of an EDS map is much lower than that of an SE or BSE image, see Figure 3.10.

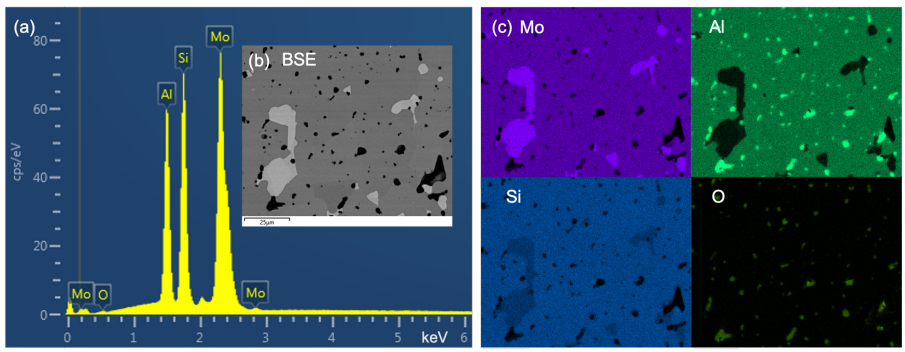

Figure 3.10: (a) Energy spectrum of $Mo(Si,Al)_2$. (b) BSE image, (c) EDS maps (Mo, Al, Si and O) of the same region

Electron backscatter diffraction

As mentioned above, EDS and BSE imaging can be used to distinguish grains having different chemical compositions, from each other. However, it is often

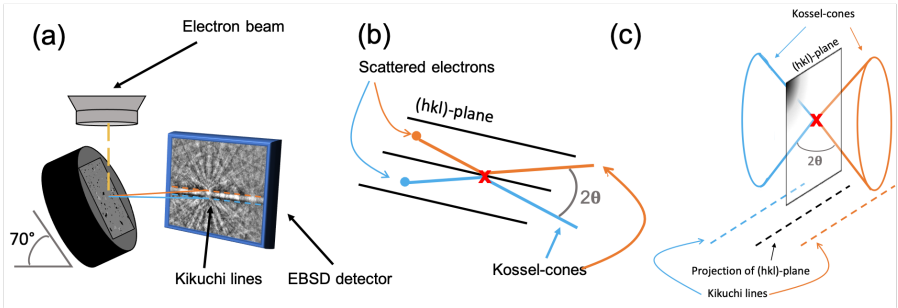

Figure 3.11: (a) The sample is placed on a 70° tilted stage under the electron beam. The Kikuchi patterns are detected by a CCD camera behind the detector. (b) and (c) show the scattering of electrons in the sample and the generation of Kossel cones

more difficult to see individual grains of the same phases. This can be done using EBSD (Electron Backscatter Diffraction).

In contrast to the other SEM-based methods, the sample is mounted on a tilted (typically 70°) stage, see Figure 3.11(a). When the sample is illuminated by the electron beam, a pattern is observed on a detector. The detector consists of a phosphor screen and a CCD camera. When the electron beam interacts with the material electrons are scattered from a point within the material. Some of these electrons are diffracted by the (hkl)-planes, indicated by the x in Figure 3.11b, to which they travel at an angle θ. If the diffraction fulfills Bragg's law (Equation 3.1), two diffraction cones (called Kossel cones), separated by an angle 2θ, are created [61]. Since the angle is very small, less than 2°, the Kossel cones are detected as two parallel lines on the detector screen. The lines are often referred to as Kikuchi lines [59, 61]. As the crystal contains a number of different (hkl) planes, a pattern of intersecting Kikuchi lines, rather than just two lines, is detected on the screen. Depending on the orientation of the crystal, the pattern will change. Therefore, EBSD can be used to investigate the orientation of diffracting crystals in a material. In Figure 3.12 the pattern from two phases with crystals oriented in different ways are shown.

EBSD is also used to study microstructure deformations of a material. When Geometrically necessary dislocations (GND) [62] are present in a material, the crystal lattice is rotated. Since the local curvature of the lattice affects the diffraction of scattered electrons, EBSD can be used to measure the change in orientation within a grain [59], and thereby the presence of GNDs. Worth mention is that only GNDs, and not statistically stored dislocations (SSD, dislocation randomly trapped within the crystal [62]) can be measured in EBSD.

The EBSD data, containing information such as crystal structure, orientation (in Euler angles) and pattern quality, is saved at every pixel. Different soft-

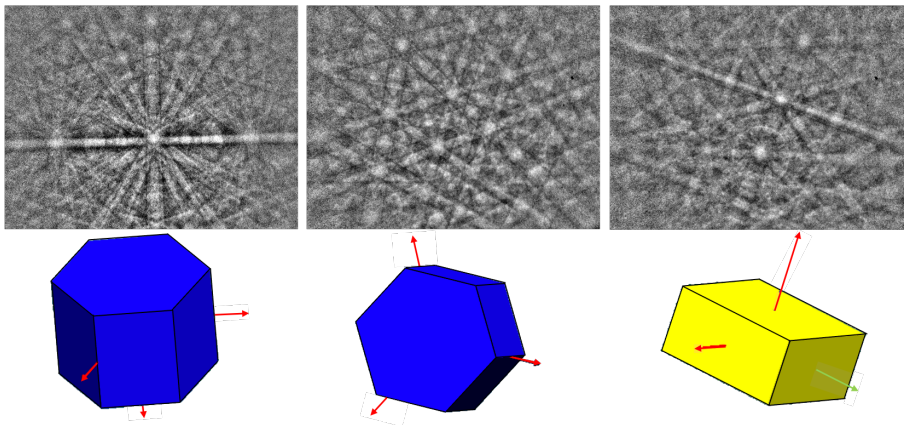

Figure 3.12: The Kikuchi pattern and orientation of two $Mo(Si,Al)_2$ and one $Mo_5(Si,Al)_3$ crystals.

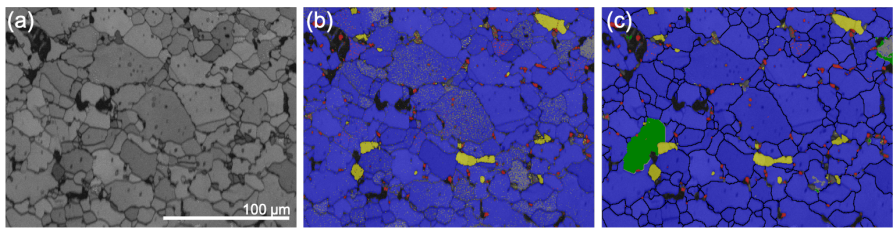

Figure 3.13: EBSD maps, (a) band contrast, (b) Phase map raw data, (c) cleaned phase map. Colours in (b) and (c): blue = $Mo(Si,Al)_2$, yellow = $Mo_5(Si,Al)_3$, red = Al_2O_3 and green = removed data

ware can then be used to process the data and create EBSD maps. The main software used in this work was Channel 5 (Oxford Instruments). The MATLAB based software MTEX [63] has been used to some extent. In the Figures 3.13 and 3.14, a number of Channel 5 based maps are shown.

The map in Figure 3.13(a) is a band contrast map, indicating the quality of the pattern. Areas having low quality, e.g. grain boundaries, pores and deformed areas, are given a lower band contrast value. In the map, dark pixels are associated with a low value. The shape and size of individual grains can easily be seen on this map. A band contrast map is often used as a background layer in other EBSD maps, see Figure 3.13(b) and (c).

The maps in Figure 3.13(b) and (c) show the different phases present in the material. The map shown in Figure 3.13(b) shows the exact indexing in every pixel. The green pixels are pixels that could not be indexed at all, which may

be due to bad quality of the Kikuchi pattern [59]. The map in Figure 3.13(c) shows the same area after cleaning the data. For the maps used in this work, the same cleaning process has been used. The first step is to replace non-indexed or incorrectly indexed isolated pixels with copies of the neighbouring pixels. In the second cleaning step, non-index areas consisting of more than one pixel are filled with information based on their neighbours. In this work, non-indexed pixels having at least five indexed neighbouring grains have been subjected to the cleaning. If the non-indexed pixel had less than five known neighbours, no cleaning was done. If the cleaning is too harsh, pores and other large non-indexed areas may be indexed incorrectly [59]. The two steps described are done by the software (Channel 5).

In a third cleaning step, small, obviously incorrectly indexed regions, were removed. This step was needed because the software had difficulties indexing some of the grains. Instead of indexing such grain as one grain, small isolated islands within that grain were indexed as many small separate grains. The incorrect grains were manually removed from the maps. In Figure 3.13(c) such regions are shown in grey (no indexing) and green (indexed but manually removed). Furthermore, at some places in the map, a few pixels are indexed as a different phase (often Al_2O_3) than the surrounding pixels (often $Mo(Si,Al)_2$). If these regions contain fewer pixels than a user-defined threshold value, they are not considered as grains and will not be in the grain list used for e.g. grain size calculations. The threshold value used in this work was 10 pixels. Figure 3.13 also shows grain boundaries having a misorientation above 10°.

The maps in Figure 3.14 are based on the orientation of the crystal. If the misorientation between every pixel within a grain and the average orientation of the grain is calculated, the grains can be assigned a GOS (Grain orientation spread) value based on the average misorientation. This has been done in the map shown in Figure 3.14(a). Grains having high GOS values are more deformed than grains having lower values.

A map based on similar calculation is the GROD (Grain Reference Orientation Deviation) map in Figure 3.14(b), where every pixel is assigned a value based on its misorientation relative to the average orientation of the grain. The misorientation is presented as an angle.

The map shown in Figure 3.14(c) is a KAM map (Kernel Average misorientation). In this map, the average misorientation between every pixel and its neighbouring pixels (within the same grain) is calculated. Regions with high local misorientation, e.g. highly deformed areas with high GND density, and low angle grain boundaries, are highlighted.

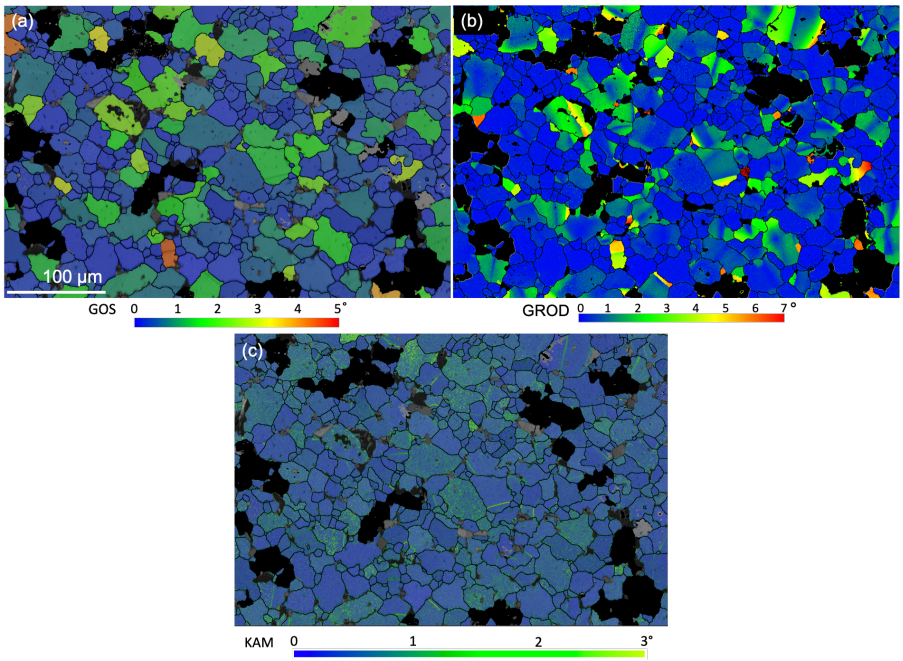

Figure 3.14: EBSD maps, (a) Grain orientation spread, (b) Reference Orientation Deviation, angle, (c) Kernel Average misorientation

CHAPTER 4

Results and Discussion

The results presented in this thesis are based on two different projects and papers. In the first paper, the effect of Y-addition on the oxidation of $Mo(Si,Al)_2$ was investigated. In the second paper, the microstructure of an unalloyed $Mo(Si,Al)_2$ material subjected to compression at 1300 °C was studied. In the following sections, the findings of the two papers will be summarised. In the first section, the microstructure of all the as-sintered materials is presented. After that, the results from the two studies are presented separately.

4.1 Initial microstructure

The synthesis of the unalloyed material used for the compression study was done by me, as a part of the PhD project. The Y-alloyed materials (containing 0, 0.1, 0,5, 1.0 and 2.0 at.% Y, respectively) for the oxidation study were synthesised prior to this project, by Kanthal. The two types of materials have been synthesised similarly, to obtain materials similar to the production material (Kanthal Super ER). However, minor parts of the process have likely become slightly different due to the change in operator and upgrades (e.g. new

equipment) in the lab. The microstructure of all synthesised materials used will be presented in this section.

Figure 4.1 shows the XRD patterns of all materials investigated in this thesis, the phases found are $Mo(Si,Al)_2$ (C40), $Mo_5(Si,Al)_3$ ($D8_m$), α-Al_2O_3. An additional phase, yttrium-aluminium-garnet (YAG, $Y_3Al_5O_{12}$), was found in the Y-alloyed material. Worth mentioning is that the C40 structure was identified using a PDF card (PDF 00-057-0374) which is based on material having the exact MoSiAl stoichiometry. Even though the material in this project had a slightly different chemical composition (see EDS results in a subsequent section), the phase was successfully indexed. The $Mo_5(Si,Al)_3$ phase was indexed using a PDF card (PDF 00-034-0371) which is based on a pure Mo_5Si_3 material. The reason why these PDF cards could be used is that the Al and Si atoms have similar atomic radii, hence, the lattice parameter is not much affected by the Al alloying, however, a slight shift in peak position can be noted, especially at high 2θ.

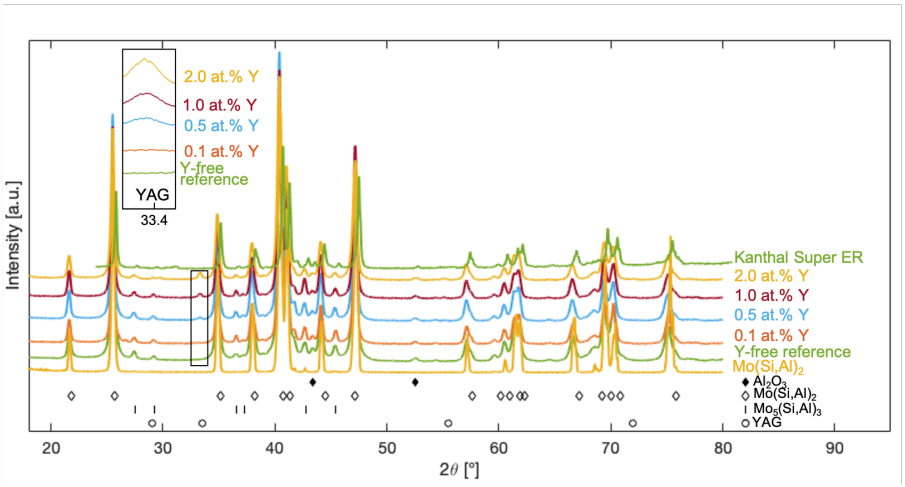

Figure 4.1: XRD pattern of the materials investigated in this thesis. From the peak close to 33.4 2θ it is shown that the YAG content increases with Y-alloying

As described in the materials synthesis section, the materials were compacted and sintered to cylindrical rods. For the microstructure investigations, the as-sintered materials were cut along the rod-axis (Figure 4.2 (a)), and the cross-section was ground using SiC paper and diamond suspensions (3 and 1 μm). The materials were investigated using SEM-based techniques, as described in section 3.3.2. Figure 4.2 shows BSE images of the material alloyed with 2 at.% Y and from the un-alloyed material from the compression study. From the BSE images, three different phases can be distinguished, $Mo(Si,Al)_2$ (I), Al_2O_3 (II) and $Mo_5(Si,Al)_3$ (III). In the Y-alloyed material, YAG grains (IV)

Table 4.1: Volume fractions of $Mo(Si,Al)_2$) materials used for the compression study and for the oxidation study. The volume fractions of $Mo(Si,Al)_2$), $Mo_5(Si,Al)_3$ and Al_2O_3 for the oxidation materials are the averages volume fractions from the Y-alloyed and reference material.

	Volume fraction (%) according to EDS		
	$Mo(Si,Al)_2$	$Mo_5(Si,Al)_3$	Al_2O_3
$Mo(Si,Al)_2$ for compression	94	3	1.7
$Mo(Si,Al)_2$ for oxidation	79	7	14
Kanthal Super ER [18]	81	6	13

can be seen as well.

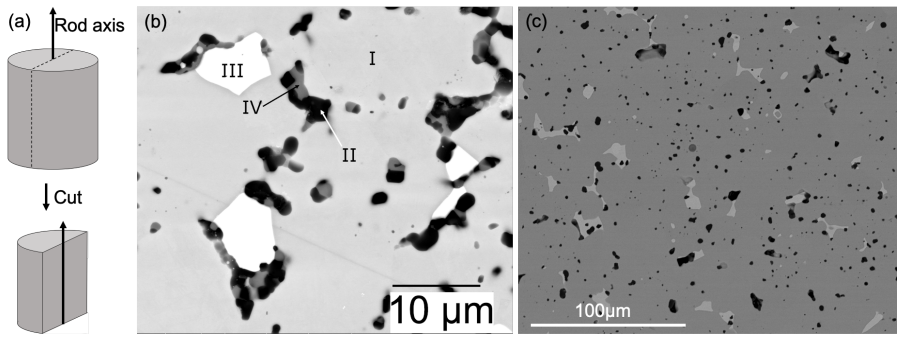

Figure 4.2: (a) Schematic figure showing how the as-sintered materials were cut for SEM analysis, BSE images of (b) 2 at.% Y alloyed material (I=$Mo(Si,Al)_2$, II=Al_2O_3, III=$Mo_5(Si,Al)_3$, IV=YAG), (c) the material used in the compression study. Note the different scale bars

The volume fractions of each material were obtained by SEM image analysis. The results are presented in Table 4.1. The Y-alloyed materials contained 0.1, 0.5, 1.4 and 2.6 vol.% YAG for the 0.1, 0.5 1.0 and 2.0 at.% alloyed materials, respectively. When comparing the two unalloyed materials (the reference material from the oxidation study and the material from the deformation study), it can be seen that material for the compression has much lower fractions of $Mo_5(Si,Al)_3$ and Al_2O_3. The difference in composition is probably due to small differences in the material synthesis. The composition of the Y-free reference material is similar to Kanthal Super ER [18].

The chemical composition of the induvidual phases was measured using EDS. In Table 4.2, the composition of the phases in the unalloyed materials used for the compression study and for the oxidation study are shown. In case of the Y-alloyed materials, Y was exclusively found in the YAG particles. In addition, the chemical composition of the Kanthal Super ER material [56] is

Table 4.2: Chemical composition of the materials used for the compression and oxidation studies, and Kantahl Super ER [56]

	$Mo(Si,Al)_2$	**$Mo_5(Si,Al)_3$**	**YAG**
	Chemical composition at.%		
$Mo(Si,Al)_2$ for compression	Mo 32.4 Si 36.6 Al 28.8 O 2.3	Mo 57.2 Si 32.6 Al 7.3 O 2.8	-
$Mo(Si,Al)_2$ for oxidation	Mo 32.1 Si 35.3 Al 29.4 O 3.2	Mo 58.5 Si 33.5 Al 5.9 O 2.2	Mo 3.5 Si 3 Al 25 O 57 Y 12
Kanthal Super ER [56]	Mo 34 Si 35 Al 27 + O	Mo 59 Si 30 Al 5 + O	-

shown. As can be seen, the chemical composition of the different materials is similar.

The $Mo(Si,Al)_2$ material used in the compression study was also investigated using EBSD. In addition to the grinding using SiC paper and diamond suspension, the surface was polished using colloidal silica. This additional step is needed because EBSD requires a mirror-like surface. Figure 4.3 shows the phase map of the as-sintered material. The average size of the $Mo(Si,Al)_2$ grains was 23 μm. The $Mo_5(Si,Al)_3$ and Al_2O_3 grains were much smaller. Only the $Mo(Si,Al)_2$ grains were studied in the compression study. The Y-alloyed materials were not investigated by EBSD.

4.2 Oxidation of Y-alloyed $Mo(Si,Al)_2$

4.2.1 Introduction

The oxidation properties of $Mo(Si,Al)_2$ based materials at high temperatures are excellent. However, on a few occasions, some spallation has been observed. The spallation leads to an increased oxidation rate and a reduced lifetime. Therefore, it is important to suppress the spallation as much as possible. In the first paper, the effect of Y additions to the $Mo(Si,Al)_2$ material has been investigated. The reason why Y was selected was that Y is used in order to improve the oxide scale adhesion in FeCrAl alloys, alumina forming alloys

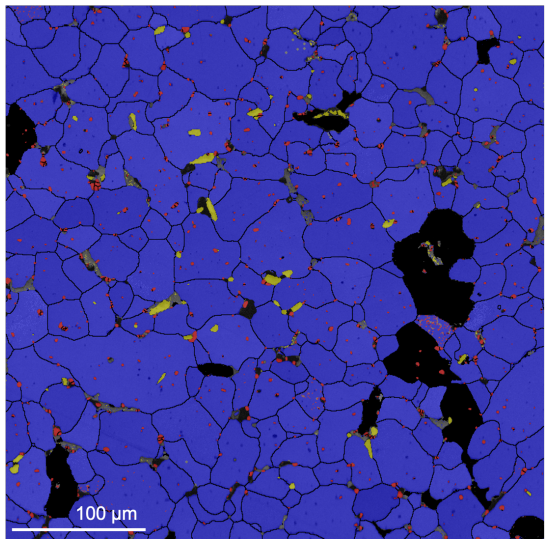

Figure 4.3: (a) Phase map of as-sintered material. Blue = $Mo(Si,Al)_2$, yellow = $Mo_5(Si,Al)_3$, red = Al_2O_3 and black = removed data

used for heating elements for temperatures up to 1250 °C. In this study, four Y-alloyed $Mo(Si,Al)_2$ materials (0.1, 0.5, 1.0 and 2.0 at.% Y, respectively) and an unalloyed material were exposed at 1500 °C, a typical temperature for $Mo(Si,Al)_2$ heating elements. The materials were weighed after 24, 50, 100 and 250 h exposure, and the microstructure of materials being oxidised for 24, 50 and 250 h was investigated using SEM.

4.2.2 Mass gain study

The mass gain study, see Figure 4.4(a), conducted at 1500 °C showed that the oxidation behaviour was severely affected by the Y-alloying of $Mo(Si,Al)_2$. In case of the unalloyed material, the mass gain curve had a parabolic shape, meaning that the material forms a protective oxide scale. The curve is in good agreement with the mass gain of Kanthal Super ER, being oxidised in dry air at 1500 °C [56]. The mass of spalled oxide (collected in alumna crucibles) was very low in case of the Y-free material, see Figure 4.4(b).

When it comes to the Y-containing materials, all samples showed mass losses (Figure 4.4(a)) and very high spallation (Figure 4.4(b)). Furthermore, the study showed that the mass loss of the Y-containing materials was not only due to spallation but also to evaporation of MoO_3, which was not much of a problem in case of the unalloyed material.

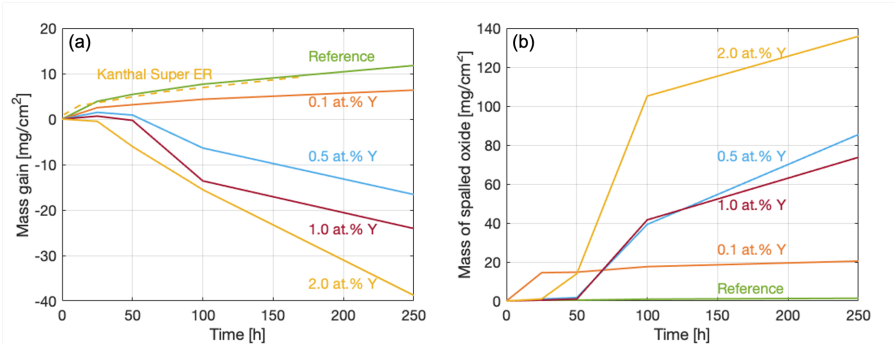

Figure 4.4: (a) Mass gain curves of the Y-alloyed materials (0, 0.1, 0.5, 1.0 and 2.0 at.% Y, respectively) and Kanthal Super ER (oxidised in dry air) [56], (b) Mass of spalled oxide from the Y-alloyed materials

4.2.3 Oxide microstructure

When cross-sections of the oxidised materials were studied in SEM, some differences were found when comparing the unalloyed and Y-containing materials. In addition to the much thicker oxide scale on the Y-containing material, these oxides contained a much higher mullite content than the scales on the unalloyed material, see Figure 4.5. Also found in the oxides were yttrium silicate (YS). YS had a dendritic structure, see Figure 4.6, which indicates that a melt has been present in the oxide scale during oxidation at 1500 °C. YS and mullite were only present in the outer part of the oxide scale, while the inner part of the oxide scale consisted of pure Al_2O_3.

Underneath the oxide scales a layer consisting of $Mo_5(Si,Al)_3$ was found. The layer is a result of preferential oxidation of the bulk material [18]. The Al content in this layer is much lower than in the $Mo_5(Si,Al)_3$ grains in the bulk material (ca 3 and 5.9 at.% Al, respectively). In case of the unalloyed material, the thickness of this layer was approximately the same as the oxide scale thickness, which is in line with previous research [18, 21, 56]. In the Y-containing materials, the thickness of the $Mo(Si,Al)_2$ layer was much thinner than the corresponding oxide scale.

The $Mo_5(Si,Al)_3$ layer has previously been explained as the source of the Si found in the oxide scale [18, 21, 56]. Small particles of the layer have been detached and incorporated in the oxide scale (see the arrow in Figure 4.5(d). With time, these particles oxidise to form SiO_2, which reacts with Al_2O_3 to form mullite, and MoO_3, which evaporates due to its high vapour pressure at elevated temperature [18, 21, 56]. Such Si and Mo particles have been found in the present study, but since no increase in size or amount of the particles

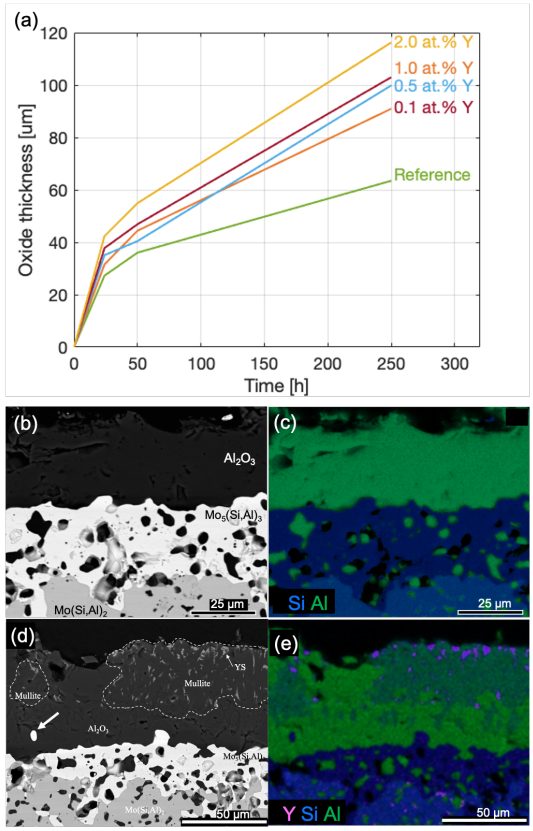

Figure 4.5: (a) Oxide thickness as a function of exposure time, (b) BSE image and (c) EDS map showing Si and Al of the unalloyed material, (d) BSE image, (e) EDS map showing Si, Al and Y of the 2 at.% Y material, oxidised for 50 h at 1500 °C the arrow in (d) shows an $Mo_5(Si,Al)_3$ grain in the oxide layer

have been found in case of the Y-containing materials, it is not likely that the thinner $Mo_5(Si,Al)_3$ and larger volume fraction of mullite in the oxide scale is due to this phenomenon alone. Instead, it is argued that Y affects the preferential oxidation of $Mo(Si,Al)_2$. This would lead to that both Si and Mo oxidise to a greater extent. As a consequence, the $Mo_5(Si,Al)_3$ will be thinner compared to the unalloyed material. How, and why Y has this effect on preferential oxidation has not been explained in the present study.

As mentioned, it is believed that a melt was present within the outer part of the oxide scales during the exposure of the Y-alloyed materials. Since oxygen can easily be transported within the melt, only the inner part of the oxide, consisting of Al_2O_3 exclusively, protects the bulk material from oxidation.

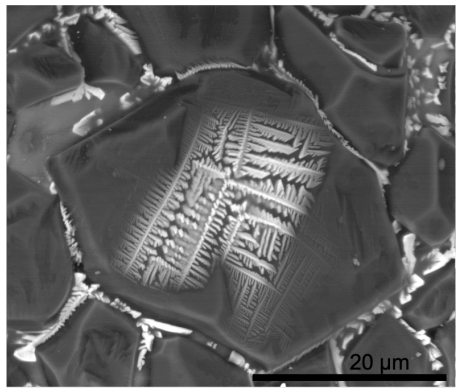

Figure 4.6: (a) BSE image of oxide surface showing the dendritic structure of YS on an Al_2O_3 grain

Therefore, it is argued that the melt is the major reason for the increased oxidation rate, which resulted in thicker oxides. The thicker oxides are also probably the reason for the pronounced spallation of the Y-alloyed materials. Due to different thermal expansion coefficients (CTE) of the oxide scale and the bulk material, stresses are introduced in the oxide during heating and cooling. If the oxide is thicker than a critical value, the oxide will spall off due to a too high stress level. Furthermore, due to the multi-phase oxide, the CTE also differs within the scale, which leads to an increased spallation.

4.2.4 Conclusions

The oxidation study clearly showed that Y addition does not improve the oxidation properties of $Mo(Si,Al)_2$. Instead, the oxidation rate increased and the material spalled severely. Therefore, Y-alloyed $Mo(Si,Al)_2$ materials can not be used for heating elements, or any other application, at elevated temperature.

The main takeaway message of this study, in addition to the new knowledge about the oxidation behaviour of the $Mo(Si,Al)_2$-Y system, is that also small additions of alloying elements may affect the oxidation behaviour. It is important to be aware of this effect when designing new $Mo(Si,Al)_2$ based materials. Even though Y was not added in order to improve the mechanical properties, it is possible that other alloying elements may have a similar effect on the oxidation properties of the material. Therefore, it is believed that the materials for future heating elements probably will be selected based on a trade-off between mechanical properties and corrosion resistance.

The study also highlights the importance of studying phase diagrams of the alloying element candidates and Mo, Si, Al and/or O prior to material synthesis. The Y_2O_3-Al_2O_3-SiO_2 phase diagram shows that there exists a molten phase at 1500 °C. It is possible that the addition of other elements also gives rise to a phase having a lower melting point than $Mo(Si,Al)_2$. Since the mechanical properties, e.g. the flow stress, in general decrease with an increase in homologous temperature (T/T_m), one would like to avoid phases with low melting temperature.

4.3 Mechanical properties of $Mo(Si,Al)_2$

4.3.1 Introduction

In the second paper, a polycrystalline $Mo(Si,Al)_2$ material was deformed at elevated temperature. While previous research has focused on single crystalline materials, this paper is, to the best of the author's knowledge, the first presenting the stress-strain curves and microstructure of a polycrystalline, deformed $Mo(Si,Al)_2$ material.

4.3.2 Compression testing

The $Mo(Si,Al)_2$ material was tested in compression at 1300 °C using a strain rate of $1{\cdot}10^{-4}$ s^{-1}. The complete testing setup is presented in the section 3.2.2.

The $Mo(Si,Al)_2$ test specimens tested in compression were plastically deformed, without crack formation and with only a slightly increase in porosity. The stress-strain curves and a photo of one of the deformed specimens are shown in Figure 4.7. The first part of the curves show that the strain increases steadily as the stress increased, this is believed to be the elastic region, with some contribution of the compliance of e.g. the anvils as explained in the "Experimental methods" section. At a compression of around 3 %, the curves start to level off and the maximum stresses, which varied between 148 and 168 MPa, were obtained shortly after. In the last part of the curves, the materials softens and the stresses required for further deformation decrease drastically.

4.3.3 Microstructure

The microstructure analysis of the tested specimen confirmed that the material had been plastically deformed. This can be observed from the much higher

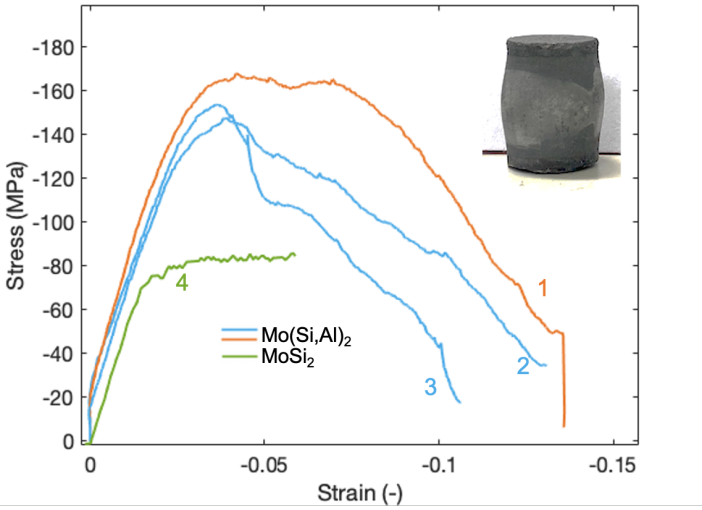

Figure 4.7: Stress-strain curves from the three polycrystalline $Mo(Si,Al)_2$ materials (curves labeled 1, 2 and 3). Specimen 1 was selected for microstructure investigation. Curve 4 is from Mitra *et al.*'s [31] compression of polycrystalline $MoSi_2$ at 1300 °C

GOS values of the grains in the deformed material compared with the grains in the as-sintered material, see Figure 4.8(a) and (b). Furthermore, three different types of grains can be observed from the KAM and GROD angle maps shown in Figure 4.8(c) and (d), respectively. The types are: (1) grains with very low deformation, (2) grains with low angle grain boundaries (LAGB), indicated by the very sharp line in the KAM map, and (3) grains having high deformation, visible as a gradual change in GROD angle.

In the two-dimensional EBSD map, the increase in GROD angle often seems to follow a specific direction, perpendicular to the [0001] axis of the grain, see Figure 4.9(a). Furthermore, the LAGBs tended to be aligned with the [0001] axis of the grain. If that is true also in the three-dimensional crystal has not been confirmed.

Due to the lack of research done on polycrystalline C40 structured silicides, the results have mainly been compared with $C11_b$ structured $MoSi_2$. Also in $MoSi_2$ the deformation was inhomogeneous and LAGBs were found in some grains [31]. Mitra *et al.* [31] argued this was due to the few slip systems operating in the $C11_b$ crystal. In the case of C40, only one slip system, $\langle 11\bar{2}0 \rangle$ (0001), is known to be active. It is therefore expected that only grains with a high Schmid factor for this slip system will undergo plastic deformation. However, in this present study, also some grains with a very low Schmid factor was de-

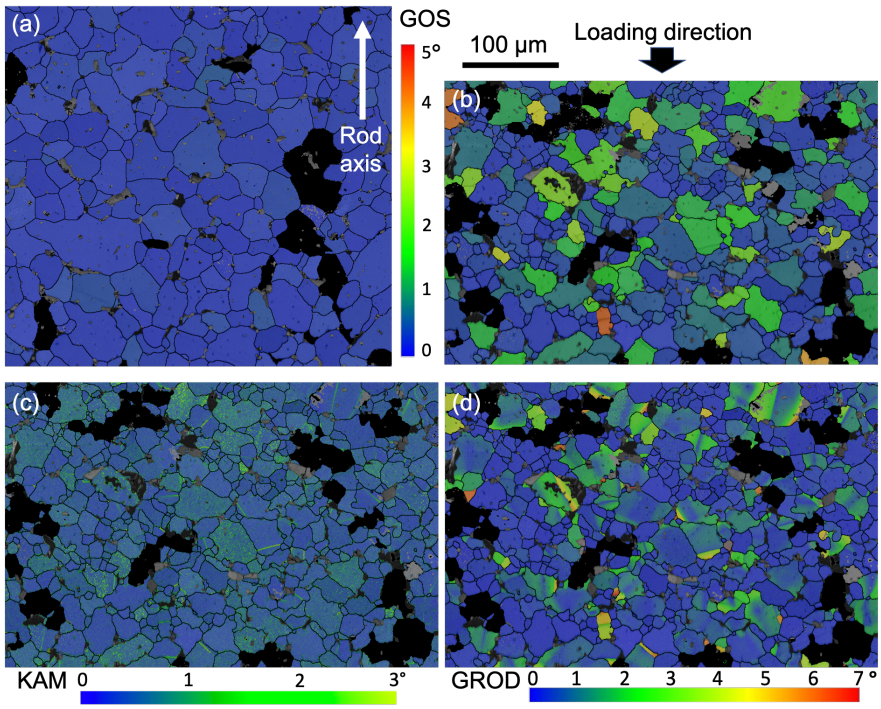

Figure 4.8: GOS maps of the (a) as-sintered and (b) deformed material, (c) KAM map, (d) GROD angle map of the deformed material. The scale bar is valid for all maps

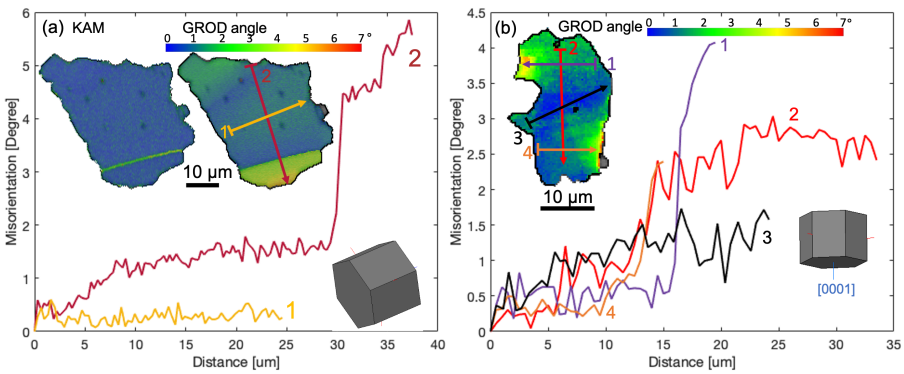

Figure 4.9: Misorientation profiles of two grains in the deformed material

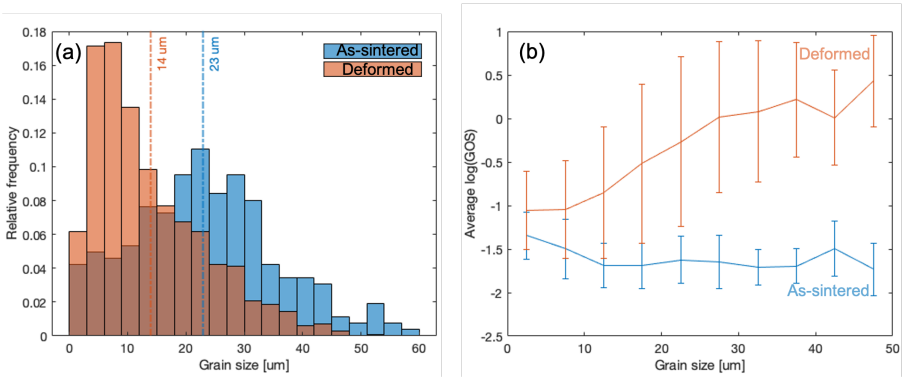

Figure 4.10: (a) Grain size distribution, (b) the logarithm of average GOS values as a function of grain size

formed, e.g. the grain shown in Figure 4.9(b). As can be seen from both the KAM map and the misorientation profiles of this grain, it is deformed very locally. It might be possible that the $\langle 11\bar{2}0 \rangle$ (0001) slip system has been activated due to stresses arising from neighbouring grains, but it is also possible that additional slip systems has been activated. Four additional slip systems have been reported in $NbSi_2$, another C40 structured silicide, when a single crystal were deformed in tension [44]. The new slip systems were found in the vicinity of a crack path where the stress state is known to be complex. In the present study, the stress state is complex due to the multiaxial stress contribution from neighbouring grains and pores, therefore, multiple slip systems may be activated in this material too. This will be further investigated using transmission electron microscopy (TEM).

Also reported was that $Mo(Si,Al)_2$ recovers by dynamic recrystallisation (DRX). DRX was not reported by Mitra *et al.* [31], but has been observed by Hardwick *et al.* [37] in the case of compression of polycrystalline $MoSi_2$ to high strains (57 %) at 1300 °C and a strain rate of 10^{-4} s^{-1}. This recovery phenomenon was shown to be sensitive to both strain rate and temperature. When comparing the stress-strain curves of $Mo(Si,Al)_2$ and Mitra *et al.*'s $MoSi_2$ material (Figure 4.7), a difference in stress behaviour is observed after yielding. While $MoSi_2$ softens only slightly (due to formation of LAGBs [31]), $Mo(Si,Al)_2$ softens considerably. Because of the limited formation of LAGBs in $Mo(Si,Al)_2$ it is not likely that softening is due to LAGB formation alone. In addition, a decrease in grain size due to deformation was observed from the EBSD data, see Figure 4.10(a) and Figure 4.8(a) and (b). Furthermore, the small grains had much lower GOS values than the large grains in the deformed material, see Figure 4.10(b). This trend was not observed in the as-sintered material, hence, it was suggested that dynamic recrystallisation takes place in the $Mo(Si,Al)_2$.

4.3.4 Conclusions

The results from this very first study investigating the microstructure of a deformed polycrystalline $Mo(Si,Al)_2$ can be summarised in three novel findings: (1) the material, which was deformed to strains of 10-15 % without crack formation, was inhomogeneous deformed both on the intragranular and intergranular scale, (2) LAGB were formed in highly deformed grains and (3) the material softens greatly after yielding as a result of LAGB formation and dynamic recrystallisation. Further research is needed in order to confirm the possible activation of additional slip systems.

CHAPTER 5

Future research

In this thesis, both oxidation and mechanical behaviour of polycrystalline $Mo(Si,Al)_2$ has been studied. Although both properties are important when developing $Mo(Si,Al)_2$ heating elements for new and more challenging applications, the focus of the remaining time of this PhD project will be on mechanical properties.

In order to better understand the deformation mechanisms taking place in $Mo(Si,Al)_2$, several new experiments are planned. In addition to test the material in compression at different temperatures, it would be interesting to stop the compression just before, and after, the initiation of softening. From such experiments, the generation of dislocations, formation of LAGB and dynamic recrystallisation could be studied in detail.

Also planned is to test the four-point bending strength of $Mo(Si,Al)_2$. This test is very relevant for the application of $Mo(Si,Al)_2$ as heating elements in large furnaces. If the elements are mounted in a horizontal position in the furnace, they will be subjected to both compressive and tensile stresses, just like in a 4-point bending test.

When the deformation behaviour of polycrystalline $Mo(Si,Al)_2$ is better understood, the world of alloying and particle strengthening of $Mo(Si,Al)_2$ materials

can be explored. As mentioned in the literature study, some C40 structured silicides show anomalous strengthening at elevated temperatures. If alloying with elements such as Nb, Ta and V could lead to an increased strength also in $Mo(Si,Al)_2$ based material, it would be very promising from an application point of view. The first step in this project is to investigate the microstructure of the alloyed material. This work has already been initiated and the materials are investigated using both in-lab analysis methods (XRD, SEM, EDS and EBSD) as well as synchrotron X-ray diffraction. Preliminary results have shown that the $Mo_5(Si,Al)_3$ phase present in the multi-phase $Mo(Si,Al)_2$ material is affected by the alloying. This phase was not given much attention in the work presented in this thesis, but the phase will indeed be thoroughly investigated in the case of alloyed materials.

Also discussed in the literature study was the improvement of strength and creep properties of $MoSi_2$ due to the addition of SiC and Al_2O_3 particles. In an ongoing project, the effect of adding Al_2O_3 particles to the $Mo(Si,Al)_2$ materials is investigated.

Bibliography

[1] The Paris Agreement - What is the Paris Agreement? https://unfccc.int/process-and-meetings/the-paris-agreement/the-paris-agreement. Accessed: 2021-11-13.

[2] CO2 and Greenhouse Gas Emissions. https://ourworldindata.org/co2-and-other-greenhouse-gas-emissions. Accessed: 2021-11-13.

[3] Forskningsprojekt 1 - Hybrit. https://www.hybritdevelopment.se/forskningsprojekt-1, Feb 2021. Accessed: 2021-11-15.

[4] S. Madeddu, F. Ueckerdt, M. Pehl, J. Peterseim, M. Lord, Karthik A. Kumar, C. Krüger, and G. Luderer. The CO2 reduction potential for the European industry via direct electrification of heat supply (power-to-heat). *Environmental Research Letters*, 15(12), 2020. doi: 10.1088/1748-9326/abbd02.

[5] Improving process heating system performance: A sourcebook for industry. United States Department of Energy, 3 edition, 2015.

[6] Sandvik Materials Technology. Resistance heating alloys for electric home appliances. www.kanthal.com/Global/Downloads/-Materialsinwireandstripform/Resistanceheatingwireandstrip/S-KA026-B-ENG-2012-01.pdf. Accessed: 2021-11-13.

[7] Sandvik Materials Technology. Kanthal Super Electric Heating Elements. https://www.kanthal.com/globalassets/kanthal-global/downloads/furnace-products-and-heating-systems/heating-elements/mosi2-heating-elements/s-ka058-b-eng-2012-01.pdf.

[8] R. W. Davidge. *Mechanical behaviour of ceramics.* Cambridge solid state science series. Cambridge U.P., 1979.

[9] R. Pampuch. *An Introduction to Ceramics.* Lecture Notes in Chemistry: 86. Springer International Publishing, 2014. doi:10.1007/978-3-319-10410-2.

[10] Z. Yao, J. Stiglich, and T. S. Sudarshan. Molybdenum silicide based materials and their properties. *Journal of Materials Engineering and Performance*, 8(3):291–304, 1999. doi: 10.1361/105994999770346837.

[11] R. Mitra. Mechanical behaviour and oxidation resistance of structural silicides. *International Materials Reviews*, 51(1):13–64, 2006. doi: 10.1179/174328006X79454.

[12] R. Mitra. *Silicides and Silicide Matrix Composites for High-Temperature Structural Applications.* 2019. doi: 10.1007/978-3-319-73255-8_40-1.

[13] H. Okamoto. Mo-Si (Molybdenum-Silicon). *Journal of Phase Equilibria and Diffusion*, 32(2):176, apr 2011.

[14] E. Ström. Mechanical properties of Mo5Si3 intermetallics as a function of composition. *Materials Characterization*, 55(4-5):402–411, nov 2005. doi: 10.1016/j.matchar.2005.09.001.

[15] R. Mitra, K. Sadananda, and C. R. Feng. Effect of microstructural parameters and Al alloying on creep behavior, threshold stress and activation volumes of molybdenum disilicides. *Intermetallics*, 12(7-9 SPEC. ISS.):827–836, 2004. doi: 10.1016/j.intermet.2004.02.033.

[16] Y. Liu, G. Shao, and P. Tsakiropoulos. Thermodynamic reassessment of the Mo-Si and Al-Mo-Si systems. *Intermetallics*, 2000. doi: 10.1016/S0966-9795(00)00068-6.

[17] T. Tabaru, K. Shobu, M. Sakamoto, and S. Hanada. Effects of substitution of Al for Si on the lattice variations and thermal expansion of Mo(Si,Al)2. *Intermetallics*, 12(1):33–41, jan 2004. doi: 10.1016/J.INTERMET.2003.07.002.

[18] L. Ingemarsson, K. Hellström, S. Canovic, T. Jonsson, M. Halvarsson, L. G. Johansson, and J. E. Svensson. Oxidation behavior of a Mo(Si,Al)2 composite at 900-1600 C in dry air. *Journal of Materials Science*, 48(4):1511–1523, 2 2013. doi: 10.1007/s10853-012-6906-0.

[19] L. Ingemarsson, M. Halvarsson, J. Engkvist, T. Jonsson, K. Hellström, L. G. Johansson, and J. E. Svensson. Oxidation behavior of a Mo (Si, Al)2-based composite at 300-1000 °C. *Intermetallics*, 2010. doi: 10.1016/j.intermet.2009.10.019.

[20] L. Ingemarsson. *Oxidation of MoSi2 based materials.* PhD thesis, Chalmers University of Technology, 2010.

[21] M. Halvarsson, T. Jonsson, L. Ingemarsson, M. Sundberg, J. E. Svensson, and L. G. Johansson. Microstructural investigation of the initial oxidation at 1450 °C and 1500°C of a Mo(Si,Al)2-based composite. *Materials at High Temperatures*, 26(2):137–143, 2009. doi: 10.3184/096034009X464195.

[22] M. F Ashby. *Materials selection in mechanical design.* Elsevier Science Technology, 5 edition, 2005.

[23] R. Mitra, V. V. Rama Rao, and A. Venugopal Rao. Effect of small aluminum additions on microstructure and mechanical properties of molybdenum di-silicide. *Intermetallics*, 7(2):213–232, feb 1999. doi: 10.1016/S0966-9795(98)00064-8.

[24] K. Ito, H. Inui, Y. Shirai, and M. Yamaguchi. Plastic deformation of MoSi2 single crystals. *Philosophical Magazine A: Physics of Condensed Matter, Structure, Defects and Mechanical Properties*, 72(4):1075–1097, 1995. doi: 10.1080/01418619508239954.

[25] A. Misra, A. A. Sharif, J. J. Petrovic, and T. E. Mitchell. Rapid solution hardening at elevated temperatures by substitutional Re alloying in MoSi2. *Acta Materialia*, 48(4):925–932, feb 2000. doi: 10.1016/S1359-6454(99)00380-8.

[26] H. Inui, M. Moriwaki, K. Ito, and M. Yamaguchi. Plastic deformation of single crystals of Mo(Si, Al)2 with the C40 structure. *Philosophical Magazine A: Physics of Condensed Matter, Structure, Defects and Mechanical Properties*, 77(2):375–394, 1998. doi: 10.1080/01418619808223759.

[27] S. A. Maloy, T. E. Mitchell, J. J. Lewandowski, and A. H. Heuer. 103¡331¿ slip in MoSi2. *Philosophical Magazine Letters*, 67(5):313–321, 1993. doi: 10.1080/09500839308241268.

[28] K. Ito, K. Matsuda, Y. Shirai, H. Inui, and M. Yamaguchi. Brittle-ductile behavior of single crystals of MoSi2. *Materials Science and Engineering A*, 261(1-2):99–105, 1999. doi: 10.1016/S0921-5093(98)01054-5.

[29] Y. Umakoshi, T. Sakagami, T. Hirano, and T. Yamane. High temperature deformation of MoSi2 single crystals with the C11b structure. *Acta Metallurgica Et Materialia*, 38(6):909–915, 1990. doi: 10.1016/0956-7151(90)90163-B.

[30] R. Gibala, A. K. Ghosh, D. C. Van Aken, D. J. Srolovitz, A. Basu, H. Chang, D. P. Mason, and W. Yang. Mechanical behavior and interface design of MoSi2-based alloys and composites. *Materials Science and Engineering A*, 155(1-2):147–158, 1992. doi: 10.1016/0921-5093(92)90322-R.

[31] R. Mitra, N. E. Prasad, S. Kumari, and A. V. Rao. High-temperature deformation behavior of coarse- and fine-grained MoSi2 with different silica contents. *Metallurgical and Materials Transactions A: Physical Metallurgy and Materials Science*, 34 A(5):1069–1088, 2003. doi: 10.1007/s11661-003-0127-8.

[32] Barry Carter C. and Grant Norton M. *Ceramic Materials: Science and Engineering*. Springer Science+Business Media, 2007. doi: 10.1007/978-0-387-46271-4.

[33] K. Sadananda, C. R. Feng, R. Mitra, and S. C. Deevi. Creep and fatigue properties of high temperature silicides and their composites. *Materials Science and Engineering: A*, 261(1):223–238, 1999. doi: https://doi.org/10.1016/S0921-5093(98)01070-3.

[34] K. Sadananda and C. R. Feng. Effect of carbon addition on the creep of molybdenum disilicide composites. *Materials Science and Engineering A*, 192-193:862–867, 1995. doi: 10.1016/0921-5093(94)03337-4.

[35] K. Huang and R. E. Logé. A review of dynamic recrystallization phenomena in metallic materials, 2016. doi: 10.1016/j.matdes.2016.09.012.

[36] T. Sakai, A. Belyakov, R. Kaibyshev, H. Miura, and J. J. Jonas. Dynamic and post-dynamic recrystallization under hot, cold and severe plastic deformation conditions. *Progress in Materials Science*, 60(1):130–207, 2014. doi: 10.1016/j.pmatsci.2013.09.002.

[37] D.A. Hardwick and P.L. Martin. Microcracking, strain rate and large strain deformation effects in molybdenum disilicide. In *MRS Proceedings: Silicides and Refractory Metals*, 1993.

[38] K. Tanaka, K. Nawata, H. Inui, M. Yamaguchi, and M. Koiwa. Temperature dependence of single-crystal elastic constants of Mo(Si,Al)2. *Intermetallics*, 6(7-8):607–611, jan 1998. doi: 10.1016/s0966-9795(98)00057-0.

[39] H. Inui and M. Yamaguchi. Deformation mechanisms of transition-metal disilicides with the hexagonal C40 structure. *Intermetallics*, 9(10-11):857–862, 2001. doi: 10.1016/S0966-9795(01)00082-6.

[40] K. Hagihara, T. Nakano, and Y. Umakoshi. Mechanical properties of C40-based ternary Mo(Si,Al)2 and quaternary (Mo,Zr)(Si,Al)2 silicides. *Scripta Materialia*, 38(3):471–476, 1998. doi: 10.1016/S1359-6462(97)00432-6.

[41] Y. Umakoshi, T. Nakano, K. Kishimoto, D. Furuta, K. Hagihara, and M. Azuma. Strength and deformation mechanism of C40-based single crystal and polycrystalline silicides. *Materials Science and Engineering A*, 261(1-2):113–121, mar 1999. doi: 10.1016/s0921-5093(98)01056-9.

[42] M. Moriwaki, K. Ito, H. Inui, and M. Yamaguchi. Plastic deformation of single crystals of NbSi2 with the C40 structure. *Materials Science and Engineering A*, 239-240(1-2):69–74, 1997. doi: 10.1016/S0921-5093(97)00562-5.

[43] H. Inui, M. Moriwaki, S. Ando, and M. Yamaguchi. Plastic deformation of single crystals of CrSi2 with the C40 structure. *Materials Science and Engineering A*, 239-240(1-2):63–68, dec 1997. doi: 10.1016/s0921-5093(97)00561-3.

[44] T. Nakano, M. Azuma, and Y. Umakoshi. Tensile deformation and fracture behaviour in NbSi2 and MoSi2 single crystals. *Acta Materialia*, 50(14):3731–3742, 2002. doi: 10.1016/S1359-6454(02)00185-4.

[45] H. Inui, M. Moriwaki, and M. Yamaguchi. Plastic deformation of single crystals of VSi2 and TaSi2 with the C40 structure. *Intermetallics*, 6(7-8):723–728, 1998. doi: 10.1016/s0966-9795(98)00045-4.

[46] K. Kishida, S. Nakatsuka, H. Nose, and H. Inui. Room-temperature deformation of single crystals of transition-metal disilicides (TMSi2) with the C11b (TM=Mo) and C40 (TM=V, Cr, Nb and Ta) structures investigated by micropillar compression. *Acta Materialia*, 223:117468, 2021. doi: 10.1016/j.actamat.2021.117468.

[47] E. W. Lee, J. Cook, A. Khan, R. Mahapatra, and J. Waldman. The oxidation resistance of MoSi2 composites. *JOM*, 43(3):54–57, 3 1991. doi: 10.1007/BF03220165.

[48] A. A. Sharif. High-temperature oxidation of MoSi2. *Journal of Materials Science*, 45(4):865–870, 2 2010. doi: 10.1007/s10853-009-4012-8.

[49] R. Mitra, V. V. Rama Rao, and Y. R. Mahajan. Oxidation behaviour of reaction hot pressed MoSi2-SiC composites at 500°C. *Materials Science and Technology*, 13(5):415–419, 1997. doi: 10.1179/mst.1997.13.5.415.

[50] K. Hansson, M. Halvarsson, J. E. Tang, R. Pompe, M. Sundberg, and J. E. Svensson. Oxidation behaviour of a MoSi2-based composite in different atmospheres in the low temperature range (400-550 °C). *Journal of the European Ceramic Society*, 24(13):3559–3573, 10 2004. doi: 10.1016/j.jeurceramsoc.2003.11.024.

[51] K. Yanagihara, K. Przybylski, and T. Maruyama. The Role of Microstructure on Pesting During Oxidation of MoSi2 and Mo(Si,AI)2 at 773 K. Technical report, 1997.

[52] Katsuyuki Yanagihara, Toshio Maruyama, and Kazuhiro Nagata. Effect of third elements on the pesting suppression of Mo-Si-X intermetallics (X = Al, Ta, Ti, Zr and Y). *Intermetallics*, 4(SUPPL. 1), 1996. doi: 10.1016/0966-9795(96)00019-2.

[53] P. J. Meschter. Low temperature oxidation of molybdenum disilicide. *Metallurgical Transactions A*, 23(6):1763–1772, 6 1992. doi: 10.1007/BF02804369.

[54] A. Stergiou, P. Tsakiropoulos, and A. Brown. The intermediate and high-temperature oxidation behaviour of Mo(Si1-xAlx)2 intermetallic alloys. *Intermetallics*, 5(1):69–81, 1997. doi: 10.1016/S0966-9795(96)00068-4.

[55] C. E. Ramberg and W. L. Worrell. Oxidation Kinetics and Composite Scale Formation in the System Mo(Al,Si)2. *Journal of the American Ceramic Society*, 85(2):444–452, 12 2004. doi: 10.1111/j.1151-2916.2002.tb00109.x.

[56] L. Ingemarsson, K. Hellström, L. G. Johansson, J. E. Svensson, and M. Halvarsson. Oxidation behaviour of a Mo(Si,Al)2 based composite at 1500 °c. *Intermetallics*, 19(9):1319–1329, 9 2011. doi: 10.1016/j.intermet.2011.05.002.

[57] Gleeble 3800-GTC. https://www.gleeble.com/products/gleeble-systems/gleeble-3800.html. Accessed: 2021-12-12.

[58] C Suryanarayana and M Grant Norton. *X-ray Diffraction - A Practical Approach*. Springer Verlag, 1 edition, 1998. doi: 10.1007/978-1-4899-0148-4.

[59] J.I. Goldstein, D. E. Newbury, J. R. Michael, N. W. M. Ritchie, J. H. J. Scott, and D. C. Joy. *Scanning Electron Microscopy and X-Ray Microanalysis*. Springer, New York, NY, 4 edition, 2018. doi: 10.1007/978-1-4939-6676-9.

[60] GIMP - Gnu Image Manipulating Program. https://www.gimp.org.

[61] David B. Williams and C. Barry Carter. *Book on Electron Microscopy*, volume 53. 2013. doi: 10.1017/CBO9781107415324.004.

[62] A. Arsenlis and D. M. Parks. Crystallographic aspects of geometrically-necessary and statistically-stored dislocation density. *Acta Materialia*, 47(5):1597–1611, 1999. doi: 10.1016/S1359-6454(99)00020-8.

[63] MTEX Toolbox. https://mtex-toolbox.github.io/.